Cooperative binding of T cell receptor and CD4 to peptide-MHC enhances antigen sensitivity

Muaz Nik Rushdi [1,2,7,11], Victor Pan[1,2,8,11], Kaitao Li [1,2,11], Hyun-Kyu Choi[1,2,11], Stefano Travaglino[1,2], Jinsung Hong[1,2,9], Fletcher Griffitts[2,3], Pragati Agnihotri[4,5,10], Roy A. Mariuzza [4,5], Yonggang Ke [1,6] ✉ & Cheng Zhu [1,2,3] ✉

Antigen recognition by the T cell receptor (TCR) of CD4+ T cells can be greatly enhanced by the coreceptor CD4. Yet, understanding of the molecular mechanism is hindered by the ultra-low affinity of CD4 binding to class-II peptide-major histocompatibility complexes (pMHC). Here we show, using two-dimensional (2D) mechanical-based assays, that the affinity of CD4−pMHC interaction is 3-4 logs lower than that of cognate TCR−pMHC interactions, and it is more susceptible to increased dissociation by forces (slip bond). In contrast, CD4 binds TCR-pre-bound pMHC at 3-6 logs higher affinity, forming TCR−pMHC−CD4 tri-molecular bonds that are prolonged by force (catch bond), and modulated by protein mobility on the cell membrane, indicating profound TCR-CD4 cooperativity. Consistent with a tri-crystal structure, using DNA origami as a molecular ruler to titrate spacing between TCR and CD4 we show that 7-nm proximity optimizes TCR−pMHC−CD4 tri-molecular bond formation with pMHC. Our results thus provide deep mechanistic insight into CD4 enhancement of TCR antigen recognition.

CD4+ T cells play vital and versatile roles in the adaptive immunity by differentiating into lineages of various functions upon activation by antigen. Antigen recognition is achieved by the T cell receptor (TCR) interacting with its cognate peptide bound to major histocompatibility complex (MHC, or pMHC when including the peptide) expressed on an antigen-presenting cell (APC) or target cell. TCR−pMHC binding triggers phosphorylation of CD3 immunoreceptor tyrosine-based activation motifs (ITAM), leading to a signaling cascade that results in T cell activation and effector function[1]. Expressed on the surface of their

respective T cell subsets, CD8 and CD4 coreceptors are thought to facilitate the initiation of the intracellular signaling cascade by stabilizing TCR−pMHC binding and delivering its associated Lck to TCR[2,3]. However, unlike CD8, CD4's extremely low affinity for MHC hinders our understanding of these proposed mechanisms that require CD4 binding to pMHC[4,5]. Indeed, surface plasmon resonance (SPR) was unable to measure CD4−MHC interactions in three-dimensions (3D)[6,7], except for one report of a ~200 μM K_d[8] that was not reproduced[6]. Although affinity measurements were successfully attained using B

[1]Wallace H. Coulter Department of Biomedical Engineering, Georgia Institute of Technology and Emory University, Atlanta, GA, USA. [2]Parker H. Petit Institute for Bioengineering and Biosciences, Georgia Institute of Technology, Atlanta, GA, USA. [3]Georgia W. Woodruff School of Mechanical Engineering, Georgia Institute of Technology, Atlanta, GA, USA. [4]W. M. Keck Laboratory for Structural Biology, Institute for Bioscience and Biotechnology Research, University of Maryland, Rockville, MD, USA. [5]Department of Cell Biology and Molecular Genetics, University of Maryland, College Park, MD, USA. [6]Medical Scientist Training Program, Emory University School of Medicine, Atlanta, GA, USA. [7]Present address: Medtronic CO., Minneapolis, MN, USA. [8]Present address: Intellia Therapeutics, Cambridge, MA, USA. [9]Present address: Food and Drug Administration, Silver Spring, MD, USA. [10]Present address: Advanced Bioscience Laboratories, Rockville, MD, USA. [11]These authors contributed equally: Muaz Nik Rushdi, Victor Pan, Kaitao Li, Hyun-Kyu Choi. ✉e-mail: yonggang.ke@emory.edu; cheng.zhu@bme.gatech.edu

cells and a supported lipid bilayer reconstituted with CD4[6], it required additional CD2–CD58 interactions to stabilize the 2D interface. The estimated 2D K_d of ~5000 μm^{-2} is >1-log higher than the K_d of TCR–pMHC interactions[9] or the CD4 density of T cell surface[10], neither of which predicts CD4–MHC interaction in vivo.

Also due to the extremely low CD4–MHC binding affinity, the ectodomain crystal structure of TCR–pMHC–CD4 tri-molecular complex was not available until a gain-of-function CD4 mutant with substantially higher affinity toward MHC was engineered[11]. Fascinatingly, the rigid coreceptor maintains a membrane-proximal spacing of ~7 nm apart from the TCR while binding to the MHC, providing an adequate gap for the missing CD3 proteins to amalgamate around the TCR[7,11,12]. The co-crystal structure suggests that the membrane-proximal positioning of TCR and CD4 ectodomains is energetically favorable to form a trimolecular complex with pMHC. Due to the differential affinities to pMHC, it is unlikely driven by the CD4 binding, but instead needs the TCR binding to pMHC to initiate the trimolecular complex formation. The above reasoning provides a rationale of our hypothesis that CD4 augmentation comes into play via its synergy with TCR, a mechanism similar to that of TCR-CD8 cooperation[13–16]. However, such cooperativity remains elusive with conflicting observations from previous studies. Our previous study using a mechanical 2D assay showed no effect of murine CD4 on murine TCR–pMHC binding under force-free conditions[10]. Studies of others using Forster Resonance Energy Transfer (FRET)[9] and pMHC tetramer staining techniques[17] failed to detect CD4 enhancement, whereas another study using Fluorescence Recovery After Photobleaching (FRAP) observed that TCR and CD4 reciprocally enhance each other's binding to pMHC[18]. Most importantly, CD4's ability to bind pMHC is still required for TCR-mediated IL-2 production even when its association with Lck is abolished[18].

Here we analyze, combining our 2D kinetic assays and mathematical modeling, the bimolecular CD4–MHC interaction and TCR-CD4 cooperativity using both purified protein ectodomains and cell systems. We identify significant cooperative binding of CD4 to TCR-prebound pMHC, which has 3–6 logs higher affinity than binding to free pMHC. By presenting TCR and CD4 on different surfaces to modulate molecular diffusion or DNA origami to modulate molecular spacing, we show that the TCR-CD4 cooperativity requires molecular mobility to allow for their colocalization within a 7-nm proximity, consistent with that reported in TCR–pMHC–CD4 tri-crystal structure. Our results explain how CD4 could efficiently augment TCR antigen recognition via cooperative binding to TCR-prebound pMHC, thereby boosting TCR sensitivity. They also underline the importance of physical factors in regulating T-cell antigen recognition, which may be imposed on molecular organization at the cell membrane via signaling-dependent and/or independent mechanisms.

Results

CD4-MHC binding displays low 2D affinity

We used our adhesion frequency assay[19,20] (Fig. 1a), which analyzes cross-junctional interactions upon initial brief cell-cell encounters, to quantify the 2D binding between HLA-DR1 presenting a melanoma antigenic peptide derived from the glycolytic enzyme triosephosphate isomerase (TPI:HLA-DR1, referred hereafter as pMHC, unless specified)[21] and its cognate E8 TCR, wild-type (WT) CD4, or a high-affinity mutant (MT) CD4 generated via directed evolution[7]. Ectodomains of each binding pair were respectively coated on two opposing RBCs, which were brought into contact and then separated to detect adhesion by RBC elongation. Results were presented as adhesion frequency (P_a) of many repeated contact-separation cycles, which was
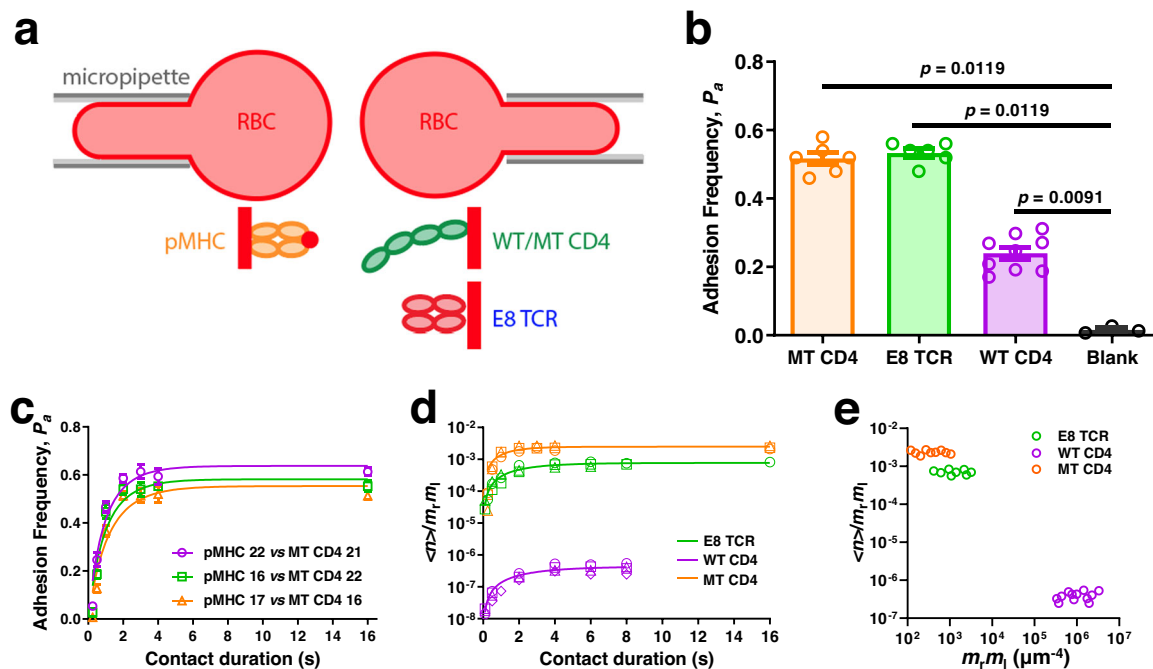
Fig. 1 | 2D kinetic analysis of TPI:HLA-DR1 interaction with E8 TCR or CD4.
a Schematics of micropipette binding frequency assay (*top*) and molecular coating (*bottom*). A pMHC-coated RBC (*left*) was repeatedly brought into contact with an opposing RBC coated with E8 TCR, or WT/MT CD4 (*right*) and separated to detect bond formation across the contact interface. **b** Specificity is shown by the significant higher (p-value indicated, by two-tailed Mann-Whitney test) of steady-state (contact time $t_c = 4$ s) adhesion frequencies (P_a, mean ± SEM ($n = 6, 6, 9, 3$ cell pairs) of indicated points each determined from 50 cycles of contact) between pMHC-coated RBCs and RBCs coated with E8 TCR, WT CD4, or MT CD4, than that without

ligand. **c** Mean ± SEM ($n = 3$ cell pairs per data point) P_a vs t_c curves for pMHC interacting with MT CD4 at various coating densities as indicated by the number in legend. **d** The normalized bond number $<n>/m_r m_l$ vs t_c curve for pMHC interaction with E8 TCR (green), WT CD4 (purple), or MT CD4 (orange). Different symbols represent independent experiments using different molecular densities that are shown in Supplementary Table 1. **e** Normalized bond number at steady-state calculated from **d** was plotted vs receptor and ligand densities. Source data are provided as a Source Data file.

Table 1 | Kinetic parameters of the purified protein system and the measurement methods

E8 TCR		CD4		Mutant CD4	
$A_c K_{a,TCR}$ (μm⁴)	Source	$A_c K_{a,CD4}$ (μm⁴)	Source	$A_c K_{a,MTCD4}$ (μm⁴)	Source
$7.70 \pm 0.40 \times 10^{-4}$	Fig. 1d	$4.35 \pm 0.49 \times 10^{-7}$	Fig. 1d	$2.48 \pm 0.15 \times 10^{-3}$	Fig. 1d
$3.01 \pm 0.69 \times 10^{-4}$	Fig. S1a	$7.74 \pm 0.60 \times 10^{-7}$	Fig. S1b	$1.30 \pm 0.26 \times 10^{-3}$	Fig. S1c
$8.31 \pm 0.46 \times 10^{-4}$	Fig. 2a,b	$4.57 \pm 1.02 \times 10^{-6}$	Fig. 3a purple	$k_{-1,MTCD4}$ (s⁻¹)	Source
$2.87 \pm 0.49 \times 10^{-4}$	Fig. 3a, green	$6.57 \pm 0.64 \times 10^{-6}$	Fig. 3d purple	0.80 ± 0.15	Fig. 1d
$3.59 \pm 0.37 \times 10^{-5}$	Fig. 3d, green	$k_{-1,CD4}$ (s⁻¹)	Source	$A_c k_{+1,MTCD4}$ (μm⁴s⁻¹)	Source
$1.42 \pm 0.46 \times 10^{-4}$	Fig. 3d, black	0.37 ± 0.11	Fig. 1d	$2.00 \pm 0.30 \times 10^{-3}$	Fig. 1d
$6.45 \pm 0.58 \times 10^{-4}$	Fig. 3h, green	4.0 ± 0.03	Fig. 2d		
$5.30 \pm 0.33 \times 10^{-4}$	Fig. 3h, black	0.84 ± 0.22	Fig. 3a purple		
$6.09 \pm 0.62 \times 10^{-4}$	Fig. 3h, orange	0.66 ± 0.08	Fig. 3d purple		
$2.02 \pm 0.18 \times 10^{-3}$	Fig. 3h, blue	$A_c k_{+1,CD4}$ (μm⁴ s⁻¹)	Source		
$8.39 \pm 1.07 \times 10^{-4}$	Fig. S2c	$1.62 \pm 0.35 \times 10^{-7}$	Fig. 1d		
$1.29 \pm 0.52 \times 10^{-5}$	Fig. 5a	$K_{a}^{*}{}_{,CD4}$ (μm²)	Source		
$k_{-1,TCR}$ (s⁻¹)	Source	$5.26 \pm 0.72 \times 10^{-2}$	Fig. 2a,b		
0.48 ± 0.07	Fig. 1d	$(8.33 \pm 4.32 \times 10^{-3})$§§	Fig. 3b, black		
0.53 ± 0.05	Fig. 2a,b	$2.69 \pm 1.14 \times 10^{-1}$	Fig. 3e, black		
11 ± 0.19	Fig. 2d	$(7.26 \pm 1.52 \times 10^{-1})$§§	Fig. 3e, brown		
0.56 ± 0.12	Fig. 3a, green	$2.99 \pm 0.27 \times 10^{-1}$	Fig. 3h, black		
0.34 ± 0.05	Fig. 3d, green	$1.0 \pm 42{,}000 \times 10^{-9}$	Fig. 3h, orange		
1.60 ± 1.06	Fig. 3d, black	$3.75 \pm 0.97 \times 10^{-1}$	Fig. 3h, blue		
0.41 ± 0.09	Fig. 3h, green	$4.87 \pm 1.07 \times 10^{-2}$	Fig. S2c		
1.11 ± 0.11	Fig. 3h, black	$5.0 \pm 1.5 \times 10^{-2}$	Fig. 5a		
0.99 ± 0.34	Fig. 3h, orange	$k_{-2,CD4}$ (s⁻¹)	Source		
(0.99 ± 0.34)§	Fig. 3h, blue	1.99 ± 1.6	Fig. 2a,b		
$A_c k_{+1,TCR}$ (μm⁴ s⁻¹)	Source	(0.12 ± 0.11)§§	Fig. 3b, black		
$3.66 \pm 0.42 \times 10^{-4}$	Fig. 1d	0.13 ± 0.12	Fig. 3e, black		
$4.38 \pm 0.48 \times 10^{-4}$	Fig. 2a,b	(10 ± 17)§§	Fig. 3e, brown		
$2.66 \pm 0.46 \times 10^{-4}$	Fig. 3h, green	4.2 ± 2.5	Fig. 3h, black		
$5.88 \pm 0.69 \times 10^{-4}$	Fig. 3h, black	2.0 ± 3.8	Fig. 3h, orange		
$6.03 \pm 2.2 \times 10^{-4}$	Fig. 3h, orange	(2.0 ± 3.8)§	Fig. 3h, blue		
$2.00 \pm 0.71 \times 10^{-3}$	Fig. 3h, blue	$k_{+2,CD4}$ (μm² s⁻¹)	Source		
		0.11 ± 0.093	Fig. 2a,b		
		0.35 ± 0.35	Fig. 3e, black		
		(7.2 ± 12)§§	Fig. 3e, brown		
		1.26 ± 0.76	Fig. 3h, black		
		$2.0 \pm 84{,}000 \times 10^{-9}$	Fig. 3h, orange		
		0.75 ± 1.4	Fig. 3h, blue		

§Use the same value as Fig. 3h, orange.

§§Two-parameter fit values.

Methods:

Figure 1d: Micropipette adhesion frequency assay with fitting to Eq. 8.

Figure 2a,b: Micropipette adhesion frequency assay with fitting to Eqs. 1 and 2.

Figure 2d: BFP thermal fluctuation assay with fitting to $\ln(p) = -k_{off}\, t$.

Figure 3a,b,d,e: BFP adhesion frequency assay with the single-species data fitting to Eq. 8 and dual-species data fitting to Eqs. 1 and 2.

Figure 3e, brown: BFP adhesion frequency assay with the black data fitting to Eqs. 1 and 2 using only two parameters ($K_{a}^{*}{}_{,CD4}$ and $k_{-2,CD4}$) after fixing $A_c K_{a,TCR}$ and $k_{-1,TCR}$ at values obtained from fitting the green and purple data by Eq. 8.

Figure 3h: Micropipette adhesion frequency assay with fitting to Eq. 8 (green curve) and Eqs. 1 and 2 (green and black curves, orange curve, and blue curve with $k_{-1,TCR}$ and $k_{-2,CD4}$ fixed at the values obtained from fitting the orange curve).

Figure 5a: Micropipette adhesion frequency assay with fitting to Eq. 4. at steady-state.

Fig. S1a–c: Micropipette adhesion frequency assay with fitting to Eq. 7 at steady-state.

Fig. S2c: Micropipette adhesion frequency assay with fitting to Eq. 3. at steady-state.

higher between RBCs functionalized with designated molecules at appropriate densities than between blank ones at the same contact time t_c, indicating specific interactions (Fig. 1b). P_a increased initially and plateaued as the probability of bond formation was balanced by that of dissociation with prolonged t_c, resulting in a steady-state (Fig. 1c). We evaluated the effective 2D affinity ($A_c K_a$) and off-rate (k_{-1}) by fitting the P_a vs t_c curve (Fig. 1c) or the log-transformed and molecular density-normalized counterparts (Fig. 1d) to a published model[19,20] (Table 1). The log transformation converts P_a to the average number of bonds per contact, $<n> = -\ln(1-P_a)$, which, after normalization by densities of the receptor (m_r) and ligand (m_l) collapses three curves measured at different $m_r \times m_l$ values (indicated by different symbols in Fig. 1d) and approaches to $A_c K_a$ at large t_c. This model was well supported as the steady-state $<n>$ increased linearly with $m_r \times m_l$

(Supplementary Fig. 1a–c) and collapsed into a single plateau upon normalization by $m_r \times m_l$ (Fig. 1e), suggesting the lack of multimeric binding and supporting the reliability of our measurements[19,20]. The effective 2D affinity of E8 TCR for pMHC ($A_c K_{a,TCR} = 7.70 \pm 0.40 \times 10^{-4}\,\mu m^4$) is comparable to, but off-rate ($k_{-1,TCR} = 0.48 \pm 0.07\,s^{-1}$) is slower than, other TCR–pMHC-II interactions[10]. Remarkably, the effective 2D affinity of CD4–MHC-II binding ($A_c K_{a,CD4} = 4.35 \pm 0.49 \times 10^{-7}\,\mu m^4$) is >3 logs lower and among the lowest values recorded[22] (Fig. 1e). Consistent with its 3D SPR measurement[7], the affinity of MT CD4 for MHC ($2.48 \pm 0.15 \times 10^{-3}\,\mu m^4$) is 3-4 logs higher than that of WT CD4 (Fig. 1e, Table 1).

TCR and CD4 cooperatively bind to pMHC

To explain how CD4–MHC binding could disproportionally recruit Lck to TCR[6], we tested the hypothesis that TCR and CD4 bind pMHC synergistically as observed for TCR and CD8[13,15,16]. E8 TCR and CD4 were co-functionalized on RBCs at different density ratios (m_{TCR}/m_{CD4}) while keeping their sum constant and tested against RBCs bearing pMHC with the same density (m_{pMHC}). We first analyzed the P_a vs t_c curves so measured (Fig. 2a) using a dual-species concurrent and independent binding model[23–25], opposite to our synergistic binding hypothesis. Without synergy, this model predicts that the average whole number of bonds $<n>_W$ would be equal to the sum of its parts, i.e., the average numbers of TCR–pMHC bonds, $<n>_{TCR}$, plus the average numbers of CD4–MHC bonds, $<n>_{CD4}$. Given the low CD4 density, which was far from enough to make up its low affinity, the measured $<n>_W$ should have yielded $<n>_{TCR}$ as its only detectable component and normalizing it by m_{TCR} and m_{pMHC} should have collapsed the entire family of curves as did Fig. 1d. Contrary to this prediction based on the dual-species concurrent and independent binding model[23–25], the $<n>_W/(m_{TCR} \times m_{pMHC})$ vs t_c curve upward shifted as m_{CD4} increased (Fig. 2b and Supplementary Fig. 2a), falsifying the independent binding assumption[23–25]. Instead of increasing linearly as in Supplementary Fig. 1, the steady-state $<n>_W$ increased nonlinearly with increasing $m_{TCR} \times m_{pMHC}$ (Supplementary Fig. 2b). Instead of being a constant as Fig. 1e, the TCR- and pMHC-density normalized whole bond number, $<n>_W/m_{TCR} \times m_{pMHC}$, increased linearly with increasing CD4 density m_{CD4} (Supplementary Fig. 2c). These results demonstrate that TCR and CD4 cooperatively bind to pMHC as we hypothesized, manifesting higher number of whole bonds than the sum of TCR–pMHC and CD4–pMHC bonds as parts.

From the difference between the whole and the sum of parts, we identified a new bond species – the emerging TCR–pMHC–CD4 trimolecular bonds whose average number is $<n>_{tri} = \Delta<n> = <n>_W - (<n>_{TCR} + <n>_{CD4})$. We developed a kinetics model in which CD4 binding of free pMHC is ignored due to its negligible affinity compared to TCR binding, but CD4 is allowed to bind TCR-prebound pMHC with a higher affinity $K^*_{a,CD4} (= k_{+2,CD4}/k_{-2,CD4})$. This model predicts (see Methods):

$$\frac{\langle n\rangle_W}{m_{TCR} m_{pMHC}} = A_c K_{a,TCR}(1 + m_{CD4} K^*_{a,CD4})$$
$$\left[1 + \frac{\lambda_2(\lambda_2 - k_{-1,TCR})e^{-\lambda_1 t_c} - \lambda_1(\lambda_1 - k_{-1,TCR})e^{-\lambda_2 t_c}}{(\lambda_1 - \lambda_2)(m_{CD4} k_{+2,CD4} + k_{-2,CD4})}\right] \quad (1)$$

where λ_1 and λ_2 are positive functions of off-rate of TCR–pMHC bond ($k_{-1,TCR}$), on- and off-rate of CD4 binding to ($k_{+2,CD4}$) and dissociating from ($k_{-2,CD4}$) TCR-prebound pMHC, and CD4 density (m_{CD4}):

$$\lambda_{1,2} = \frac{1}{2}(k_{-1,TCR} + k_{-2,CD4} + m_{CD4} k_{+2,CD4})$$
$$\pm \frac{1}{2}\left[(k_{-1,TCR} + k_{-2,CD4} + m_{CD4} k_{+2,CD4})^2 - 4k_{-1,TCR} k_{-2,CD4}\right]^{1/2}. \quad (2)$$

The steady-state solution as $t_c \to \infty$ is

$$\frac{\langle n\rangle_{W,\infty}}{m_{TCR} m_{pMHC}} = A_c K_{a,TCR} + m_{CD4} A_c K_{a,TCR} K^*_{a,CD4} \quad (3)$$

The second term on the right-hand side of Eq. 3 can be identified as the steady-state average number of trimolecular bonds $<n>_{tri}$ per densities of TCR and pMHC. Both the original (Fig. 2a) and normalized (Fig. 2b) data were well fitted by Eq. 1 & 2. Fitting returned values of $A_c K_{a,TCR} = 8.31 \pm 0.46 \times 10^{-4}\,\mu m^4$ and $k_{-1,TCR} = 0.53 \pm 0.05 \times s^{-1}$ for the TCR–pMHC interaction from the dual receptor species experiment in the presence of CD4, which agree well with the previous single receptor species experiment in the absence of CD4 (Table 1). Remarkably, the value of $K^*_{a,CD4}$ is $0.0526 \pm 0.0072\,\mu m^2$, >250 times higher than the previous value obtained using CD4-reconstituted supported lipid bilayers[6] and >350,000 times higher than the CD4 affinity for free pMHC calculated by dividing the $A_c K_{a,CD4}$ value determined from Fig. 1d by the ~3 μm^2 contact area A_c estimated from the side-view microscopic image.

To visualize the emergence of TCR–pMHC–CD4 trimolecular bonds, we transformed the data according to Eq. 3: subtracting the black data set ($m_{CD4} = 0$) from the colored data sets ($m_{CD4} > 0$) and normalizing them by their corresponding CD4 density. This nearly collapses the three colored data sets into the average number of trimolecular bonds per unit densities of TCR, pMHC, and CD4. This $<n>_{tri}/(m_{TCR} \times m_{pMHC} \times m_{CD4})$ data vs contact time t_c plot compares well with our model prediction using the best-fit kinetic parameters obtained earlier, showing how the degree of cooperativity increase in time until reaching the steady-state value $A_c K_{a,TCR} K^*_{a,CD4}$ (Fig. 2c). Thus, the steady-state trimolecular bond number per unit density of TCR, CD4, and pMHC is equal to the product of the effective 2D affinity of the TCR–pMHC bond and the 2D affinity of CD4 for TCR-prebound pMHC, an intuitive result that makes very good sense.

TCR–pMHC–CD4 trimolecular bond shows a much greater catch than TCR–pMHC bimolecular bond

To examine whether the trimolecular bond can better sustain mechanical force, we used the biomembrane force probe (BFP) thermal fluctuation[20,26] and force-clamp[10,16,27] assays to measure respective force-free and force-dependent lifetimes of single bonds between glass beads bearing pMHC and targets presenting ectodomains of E8 TCR, CD4, or both mixed at a 1:1 concentration ratio. The thermal fluctuation assay yielded fairly linear survival probability vs bond lifetime semi-log plots for dissociation of single-receptor species (TCR or CD4) and dual-receptor species (TCR and CD4) from TPI: HLA-DR1, which were much longer lived than the negative control 9V:HLA-A2 (Fig. 2d), conforming binding specificity of TCR and/or CD4.

The force-clamp assay found the CD4–MHC bond lifetimes to decrease with increasing force, displaying a slip-only bond behavior[10,16,27,28] (Fig. 2e). The TCR–pMHC interaction, in contrast, behaved as a catch-slip bond where the lifetime increased, reached a peak, and decreased in a biphasic fashion as force increased[10,16,27,28] (Fig. 2e). Remarkably, the interactions between pMHC probes and targets co-presenting TCR and CD4 exhibited a much more pronounced catch-slip bond (Fig. 2e). Since lifetimes were measured at infrequent binding (<20%) to ensure >89% single-bond probability, the "whole" lifetime ensemble included subpopulations of single TCR–pMHC, CD4–MHC, and TCR–pMHC–CD4 bond lifetimes, where the whole lifetime represented a weighted sum of all three contributions. Average lifetimes of whole bonds were much longer than the weighted sum of two parts—the average lifetimes of TCR–pMHC and CD4–MHC bonds—regardless of how their relative weights were adjusted (Fig. 2e), as it cannot be longer than the longer component lifetime of the two. This demonstrates the existence of a more "catchy" and longer-lived trimolecular bond species.
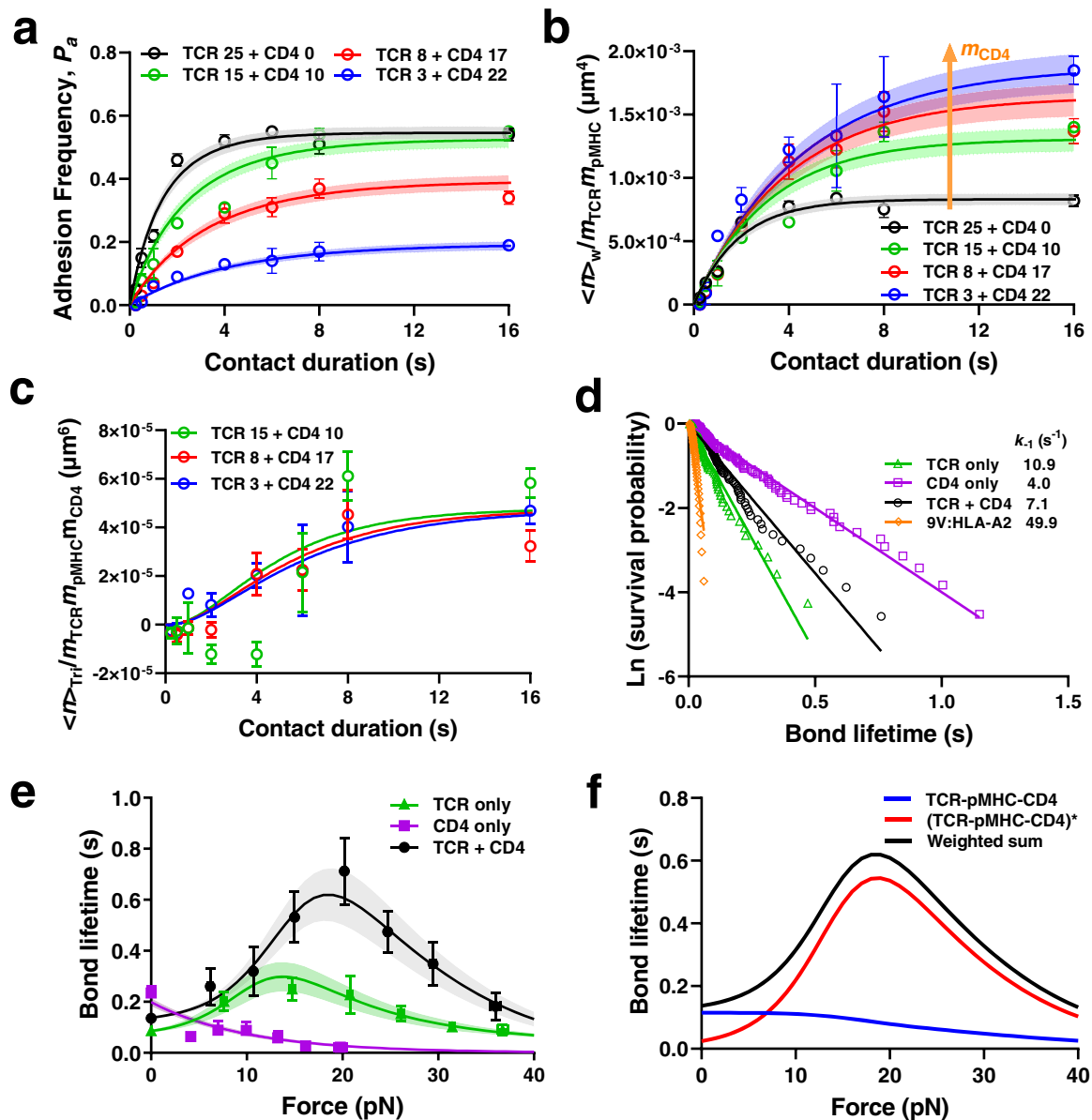
Fig. 2 | Ectodomains of TCR and CD4 bind cooperatively to pMHC. a P_a vs t_c data (points, presented as Mean ± SEM) and their model fits (curves) of pMHC-coated RBCs (38 μm^{-2}) binding to RBCs coated with TCR alone, or a mixture of TCR and CD4 at densities (# of molecules/μm^2) indicated by the numbers in legend. **b** Normalized whole bond number $\langle n \rangle_w/m_{TCR}m_{pMHC}$ vs t_c data (points, presented as Mean ± SEM) and their respective model fits (curves) for interactions in **a**. Arrow indicates decreasing density of TCR and increasing density of CD4. **c** Normalized trimolecular bond number $\langle n \rangle_{tri}/m_{TCR}m_{pMHC}m_{CD4}$ vs t_c data (points, presented as Mean ± SEM) and their respective model fits (curves) calculated from **b** by subtracting the black data from colored data followed by further normalization by m_{CD4}. **d** Survival probabilities plotted as ln(# of events with lifetime greater than t) vs. bond lifetime for pMHC-coated beads interacting with beads coated with TCR, CD4, or a 1:1 mixture of TCR and CD4 measured by BFP thermal fluctuation at zero

force. Each data set (points) was fitted by a straight line with the negative slope representing off-rate for TCR ($k_{-1,TCR}$, $n = 71$) or CD4 ($k_{-1,CD4}$, $n = 92$), or apparent off-rate for the mixed TCR and CD4 ($n = 97$). As a negative control, class-I MHC 9 V:HLA-A2 was used instead of TPI:HLA-DR1 to measure non-specific binding ($n = 42$). **e** Mean ± SEM bond lifetime vs force data (points), measured by BFP force-clamp experiment using beads bearing TPI:HLA-DR1 interacting with E8 TCR ($n = 230$), CD4 ($n = 355$), or a 1:1 mixture of E8 TCR and CD4 ($n = 424$) coated on beads, are compared with theoretical curves (mean ± SE) predicted using the model and best-fit parameters in Supplementary Fig. 3. **f** Model predicted trimolecular bond lifetime vs force plots for strong (red) and weak (blue) states as well as their sum (black). Data in **a**–**c** were from two independent experiments for each curve. Their model fits (mean ± SE) were calculated using Eqs. 1 and 2 based on the best-fit parameters listed in Table 1. Source data are provided as a Source Data file.

We used a single-state, single-pathway dissociation model for the slip-only bonds of CD4–MHC interaction and two two-state, two-pathway dissociation models for the catch-slip bonds of the respective TCR–pMHC and TCR–pMHC–CD4 interactions (Supplementary Fig. 3a) to globally fit the measured lifetime vs force scattergrams (Supplementary Fig. 3b). The models fit the mean ± SE bond lifetime vs force data well (Fig. 2e) and predict the probability and fraction of strong state of TCR–pMHC and TCR–pMHC–CD4 bonds (Supplementary Fig. 3e–h) as well as the average bond lifetime vs force curves

of the strong state, weak state, and their sum (Fig. 2f), which reveals how the TCR–pMHC–CD4 bond is activated to a strong state by force to form a cooperative catch bond.

TCR-CD4 cooperativity on cells

We performed two sets of experiments to confirm that the TCR-CD4 cooperativity observed using purified ectodomain proteins was operative when these proteins were expressed on cells. First, we analyzed binding of beads coated with E8 TCR, CD4, or both to THP-1 cells

pulsed with TPI peptide after stimulation with IFN-γ to upregulate HLA-DR1 expression[21]. Analyses of adhesion frequency P_a (Fig. 3a) and of the corresponding normalized bond number $<n>_W/m_{Receptor} \times m_{pMHC}$ (Fig. 3b) mediated by the TCR–pMHC (green) and CD4–MHC (purple) bimolecular interactions yielded $A_cK_{a,TCR} = 2.87 \pm 0.49 \times 10^{-4}\ \mu m^4$ and $A_cK_{a,CD4} = 4.57 \pm 1.02 \times 10^{-6}\ \mu m^4$. The former value is a comparable to, and the latter value is a log higher, than the corresponding values of TCR and CD4, respectively, for the purified MHC.

When tested against beads coated with both TCR and CD4, the P_a (Fig. 3a, black) and the corresponding normalized whole bond number $<n>_W/m_{TCR} \times m_{pMHC}$ (Fig. 3b, black) were much higher than the predicted the sum of TCR–pMHC and CD4–MHC interactions calculated using our measured kinetic rates and molecular densities (Fig. 3a, b, dashed curves), demonstrating that purified TCR and CD4 cooperatively bind cellular pMHC. Interestingly, fitting the dual species data to Eq. 1 & 2 while holding the TCR–pMHC and CD4–MHC kinetic rates the same values as in their bimolecular interactions yielded a good fit of the data with $K^*_{a,CD4} = 8.33 \pm 4.32 \times 10^{-3}\ \mu m^2$, which is 0.16 times of that obtained using purified pMHC (Fig. 2a, b). Assuming a contact area of 1 μm², the affinity of CD4 binding to TCR-engaged pMHC is ~1,823 fold of that for free pMHC. This fold increase is smaller than that obtained using purified pMHC and is likely due to the fact that in this case TCR and CD4 are immobilized on BFP beads instead of being freely diffusible on the RBC membrane.

To further confirm TCR-CD4 cooperativity for cellular pMHC, we measured bond lifetime vs force curves, finding that THP-1 expressed TPI:HLA-DR1 formed a slip-only bond, weak catch-slip bond, and strong catch-slip bond with beads coated with CD4 only, E8 TCR only, and both E8 TCR and CD4, respectively (Fig. 3c), consistent with the results obtained using purified pMHC (Fig. 2e).

Next, we analyzed purified pMHC binding to cellular TCR and CD4, and quantified the impacts of their transmembrane and cytoplasmic domains and of the CD3 signaling chains, which the purified TCRαβ and CD4 ectodomains lack and have been shown important in our previous studies of TCR-CD8 cooperativity[13,16], on TCR-CD4 cooperativity. We performed experiments using Jurkat cells transfected with, and sorted to express comparable levels of E8 TCR, CD4, or both. We first analyzed the P_a vs t_c curves of these Jurkat cells binding to TPI:HLA-DR1 coated bead using the BFP setup (Fig. 3d). Comparing to purified TCRαβ coated on RBCs, cellular TCR-CD3 complex exhibits a ~1 log lower effective 2D affinity ($A_cK_{a,TCR} = 3.59 \pm 0.37 \times 10^{-5}\ \mu m^4$). In contrast, despite the smaller functional contact area, cellular CD4 has an effective 2D affinity ($A_cK_{a,CD4} = 6.57 \pm 0.64 \times 10^{-6}\ \mu m^4$) for purified pMHC that is ~1 log higher than that of purified CD4 for purified pMHC and similar to that of purified CD4 for cellular pMHC (Table 1).

Similar to the cell-free system, measurements with cells expressing both TCR and CD4 showed significantly higher adhesion frequency P_a (Fig. 3d, black) and normalized whole bond number $<n>_W/m_{TCR} \times m_{pMHC}$ (Fig. 3e, black) than the predicted the predicted sum mediated by the sum of TCR–pMHC and CD4–MHC interactions calculated using their measured kinetic rates and molecular densities (Fig. 3d&e, dashed curve), demonstrating that cellular TCR and CD4 cooperatively bind purified pMHC.

Comparing the predicted curve of Eq. 1 & 2 with the $<n>_W/m_{TCR} \times m_{pMHC}$ vs t_c measurement showed excellent agreement between the model and data in both the logarithmic transformed variable (Fig. 3e) and the directly measured variable (Fig. 3d). Fitting the data returned values of $K^*_{a,CD4} = 0.269 \pm 0.114\ \mu m^2$ and $k_{-2,\ CD4} = 0.131 \pm 0.117\ s^{-1}$, respectively, of and ~1 log smaller than the corresponding values estimated from the cell-free system (Table 1). Interestingly, the values of $A_cK_{a,TCR} = 1.42 \pm 0.463 \times 10^{-4}\ \mu m^4$ and $k_{-1,TCR} = 1.60 \pm 1.06\ s^{-1}$ estimated from fitting the $<n>_W/m_{TCR} \times m_{pMHC}$ data are, respectively, 4 and 4.7 times of the counterpart values

estimated from fitting the respective $<n>_{TCR}/m_{TCR} \times m_{pMHC}$ and $<n>_{CD4}/m_{TCR} \times m_{pMHC}$ data. This is in contrast to both the results obtained by fitting the purified TCR-CD4 vs purified and cellular pMHC data where the corresponding numbers match (Table 1). Indeed, fitting the same whole bond data by Eq. 1 & 2 using the $A_cK_{a,TCR}$ and $k_{-1,TCR}$ values estimated from single bond species measurements as given rather than free fitting parameters resulted in a poor fit of significantly slower kinetics than the actual data (Fig. 3e brown curve), in sharp contrast to the excellent fits in Fig. 2b and 3b where the $<n>_W/m_{TCR} \times m_{pMHC}$ curve and the $<n>_{TCR}/m_{TCR} \times m_{pMHC}$ curve have common initial slope at $t_c = 0$, as predicted by Eq. 1 & 2. To compensate for the pre-determined lower $A_cK_{a,TCR}$ and slower $k_{-1,TCR}$ values, the two-parameter fit (Fig. 3e brown curve) required much higher affinity ($K^*_{a,CD4} = 0.726 \pm 0.152\ \mu m^2$) and off-rate ($k_{-2,\ CD4} = 10.0 \pm 16.9\ s^{-1}$) for CD4 to respectively bind to and dissociate from TCR-prebound pMHC as compared to the four-parameter fit (Fig. 3e black curve). These results reveal similarities and distinctions between the cellular and purified TCR-CD4 systems and suggest that intracellular regulations, which are absent in the purified TCR-CD4 system but present in the cellular TCR-CD4 system, may speed up the first-stage kinetics to allow CD4 to cooperate in pMHC binding at an earlier time, a contention consistent with our previous results that intracellular regulations is important to the TCR-CD8 cooperative binding of class-I pMHC[13,16].

Cellular TCR-CD4 cooperativity was also confirmed in bond lifetime analysis: TPI:HLA-DR1 formed a slip-only bond, weak catch-slip bond, and strong catch-slip bond with cells expressing CD4 only, E8 TCR only, and both E8 TCR and CD4, respectively, similar to their purified protein counterparts (Fig. 3f). In addition, Jurkat cells expressing a higher level of TCR than CD4 formed a more pronounced catch bond than those express similar levels of TCR and CD4 (Fig. 3f), suggesting a higher degree of cooperativity.

As an additional confirmation, we analyzed CD4+CD8- and CD4-CD8+ single-positive T cells[29] from 3.L2 TCR transgenic mice, which recognizes a hemoglobulin (Hb) epitope presented by mouse class-II pMHC I-E^k (Hb:I-E^k)[10]. Our previous adhesion frequency experiment was unable to detect mouse CD4–Hb:I-E^k binding, indicating an $A_cK_{a,CD4} < 7.0 \times 10^{-8}\ \mu m^4$ (the detection limit), no less than a log lower than the human CD4–HLA-DR1 effective 2D affinity, and observed a TCR–pMHC catch-slip bond between BFP probes bearing Hb:I-E^k and CD4-CD8+ 3.L2 T cells by force-clamp BFP experiment[10]. Interestingly, when using CD4+CD8- T cells we observed a much more pronounced catch-slip bonds, which was suppressed by anti-CD4 (GK1.5) blocking to the level of using CD4-CD8+ T cells (Fig. 3g). These data confirm that the prolonged lifetimes were CD4-dependent and further support the formation of more durable and force-resistant TCR–pMHC–CD4 trimolecular bonds by TCR-CD4 cooperation.

TCR-CD4 cooperativity requires molecular mobility

The faster kinetics of the cellular TCR-CD4 cooperative binding to pMHC (Fig. 3e) may suggest enhanced CD4 recruitment to TCR–pMHC, a process that requires both molecular mobility and proximity. To test whether cooperativity depends on molecular diffusion, we used four different pairings of surfaces to present proteins: (1) pMHC on RBCs interacting with TCR only on RBCs; (2) pMHC on RBCs interacting with TCR and CD4 on RBCs; (3) pMHC on RBCs interacting with TCR and CD4 on beads; and (4) pMHC on beads interacting with TCR and CD4 on RBCs. The idea is to allow lateral diffusion of TCR and CD4 on the RBC membrane but prevent them from doing so on the bead surface. The data were presented as average number of whole bonds per unit densities of TCR and pMHC as in Fig. 2b. When interacting proteins on both sides were coated on RBCs (2nd pairing), pMHC interaction with TCR-CD4 dual-receptor species (Fig. 3h, black) generated a much higher $<n>_W/(m_{TCR} \times m_{pMHC})$ curve than did with TCR single-receptor species (Fig. 3h, green), indicating cooperative binding as in Fig. 2b. In
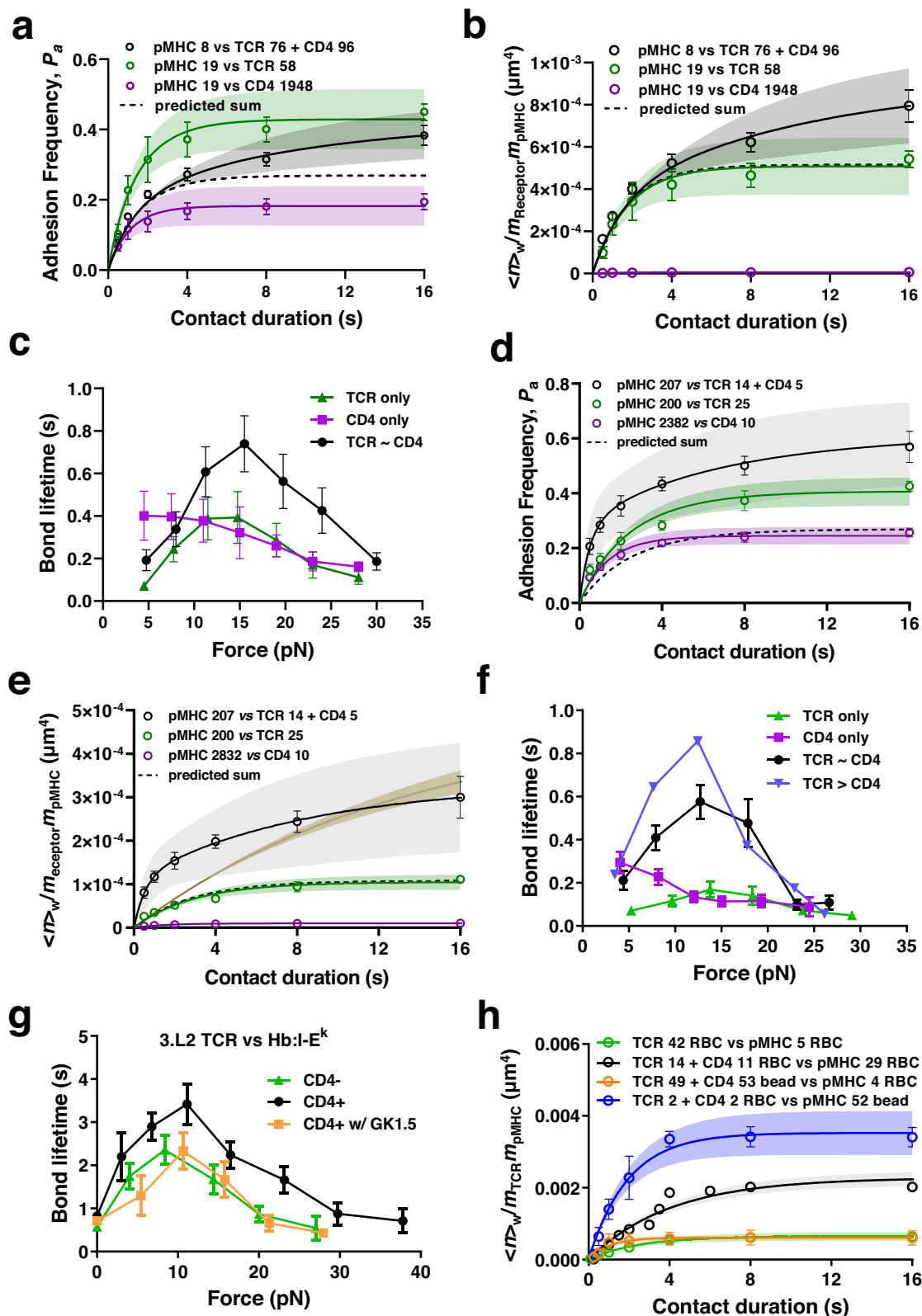
sharp contrast, when pMHC was coated on RBCs and TCR and CD4 were co-functionalized on beads (3rd pairing), the binding curve was substantially downward shifted to the level indistinguishable to the curve generated by coating TCR-only on RBCs binding to RBCs bearing pMHC (1st pairing, Fig. 3h, orange). This indicates that the cooperativity between TCR and CD4 vanished when they were immobilized at low densities on glass bead surface. When pMHC

was coated on beads and the TCR/CD4 mixture was coated on RBCs (4th pairing), the binding curve was upward shifted to a level higher than that resulted from coating proteins from both sides on RBCs, as predicted by the lower CD4 density (Fig. 3h, blue).

Using Eq. 1 & 2 to globally fit the green and black data (Fig. 3h) returns $A_cK_{a,TCR}$ and $k_{-1,TCR}$ values comparable to, and $K_{a,CD4}^*$ and $k_{-2,CD4}$ values even larger than, those obtained by fitting Fig. 2b

Fig. 3 | Cellular TCR and CD4 bind cooperatively to pMHC. a P_a vs t_c data (Mean ± SEM of 3-6 cells per data point) and their model fits (curves) of TPI-pulsed IFN-γ treated THP-1 cells binding to beads presenting TCR, CD4, or both at densities (μm^{-2}) indicated in the legends. **b** Normalized whole bond number $\langle n \rangle_w/m_{Receptor}m_{pMHC}$ vs t_c data (points, presented as Mean ± SEM) and their respective model fits (curves) for interactions in **a**. **c** Mean ± SEM bond lifetime vs force data of TPI-pulsed IFN-γ treated THP-1 cells interacting with beads presenting E8 TCR ($n = 201$), CD4 ($n = 200$), or E8 TCR and CD4 of similar density ($n = 225$). **d** P_a vs t_c data (Mean ± SEM of 3-7 cells per point) and their model fits (curves) of pMHC-coated beads binding to Jurkat cells expressing TCR, CD4, or both at densities (μm^2) indicated by the legends. **e** Normalized whole bond number $\langle n \rangle_w/m_{Receptor}m_{pMHC}$ vs t_c data (points, presented as Mean ± SEM) and their respective model fits (curves) for interactions in **d**. Predications were made after normalizing the densities in different curves. TCR + CD4 curve was fitted with (brown) or without (black)

keeping the same TCR affinity and off-rate as in the bimolecular interaction. **f** Mean ± SEM bond lifetime vs force data of BFP beads bearing TPI:HLA-DR1 interacting with Jurkat cells expressing E8 TCR ($n = 598$), CD4 ($n = 283$), E8 TCR and CD4 of similar density ($n = 279$) or more TCR than CD4 ($n = 288$) expressed on Jurkat cells. **g** Mean ± SEM bond lifetime vs force data of BFP beads bearing Hb:I-E^k interacting with 3.L2 CD8$^+$CD4$^-$ T cells ($n = 298$), CD8$^-$CD4$^+$ T cells ($n = 711$), or CD8$^-$CD4$^+$ T cells with CD4 blocking antibody clone GK1.5 ($n = 240$). **h** Comparison among normalized bond numbers for pMHC interaction with TCR or mixed TCR and CD4 coated in four ways at densities (# of molecules/μm^2) indicated by the number in legend. Data (points) are presented as mean ± SEM of two independent experiments for each curve. Their model fits (mean ± SE curves) are calculated using Eqs. 1 and 2 based on the best-bit parameters listed in Table 1. Source data are provided as a Source Data file.

(Table 1). In sharp contrast, fitting the orange data (Fig. 3h) returns a vanishingly small 2D affinity of CD4 for TCR-prebound pMHC $K_{a,CD4}^*$ (1.0×10^{-9} μm^2) with a 4-log larger standard error (4.2×10^{-5} μm^2) despite reasonable values of $A_cK_{a,TCR}$, $k_{-1,TCR}$, and $k_{-2,CD4}$ (Table 1). Fitting the blue data (Fig. 3h) after constraining $k_{-1,TCR}$, and $k_{-2,CD4}$ to prevent over-fitting generated $A_cK_{a,TCR}$ and $K_{a,CD4}^*$ values similar to those obtained by globally fitting the green and black data (Table 1). Together, these results indicate that cooperative trimolecular interaction was modulated by the mobility of TCR and CD4 on the cell surface.

Optimal TCR-CD4 cooperativity is achieved at 7 nm spacing

We hypothesized that the mobility effect might stem from the requirement for sparsely distributed TCR and CD4 to diffuse into close proximity for them to physically reach the same pMHC. To test this hypothesis, we designed a DNA nanostructure – a ~250-nm 10-helix bundle (10HB) DNA origami nanorod[30], which can be used as a molecular ruler for precise control of the arrangement and relative locations of proteins[30]. 10HB nanorods functionalized with TCR and CD4 were captured on a magnetic bead to form a surrogate T cell (Fig. 4a) to test against a pMHC bearing RBC in the 2D kinetic assay (Fig. 4b). Many poly-A DNA strands protrude from one side of 10HB to bind poly-T strands on the bead surface, while TCR and CD4 are anchored by "capture" DNA strands on the other side of 10HB (Fig. 4c). The position of the capture DNA strands was changed to adjust the TCR-CD4 intermolecular spacing, which was designed to be 6, 13, 20, and 100 nm for this study (Fig. 4d). To bind the proteins to their complementary capture DNA strands on 10HB, CD4 was covalently linked with a DNA strand, verified by sodium dodecyl-sulfate polyacrylamide gel electrophoresis (SDS PAGE) (Fig. 4e). C-terminally biotinylated E8 TCR was bound to a streptavidin (SA), which was in turn bound to a biotinylated DNA strand on the 10HB (Fig. 4c). Successful assembly of 10HB nanorods was confirmed via native agarose gel electrophoresis (Fig. 4f). A slight decrease in mobility was observed after the addition of single-stranded extensions (poly-T strands and capture strands), compared to naked 10HB nanorods. The nanorods were extracted from the gel bands, purified, and used for attachment of TCR and CD4. Subsequent transmission electron microscopy imaging on negatively stained samples clearly showed the binding of TCR and CD4 and their 13-nm and 20-nm designed intermolecular spacings (Fig. 4g). We should note that the designed spacing are nominal, as the actual spacing can be affected by the length of DNA handles, the size of streptavidin, and the flexibility of the linkage.

To examine how TCR-CD4 spacing impacted their synergistic binding to pMHC, we measured adhesion frequencies between RBCs bearing pMHC and origami beads coated with E8 TCR, CD4, or both with defined spacing. CD4-alone origami adhered negligibly as did protein/handle negative or origami negative controls, whereas the same density of TCR-alone origami yielded ~20% of P_a at steady-state ($t_c = 4$ s), consistent with its >3 logs higher affinity (Supplementary

Fig. 4). Multiplexing TCR and CD4 on the origami 100 and 20 nm apart generated indistinguishable adhesions comparable to the TCR-alone group. Strikingly, further decreasing the spacing to 13 and 6 nm profoundly increased P_a (Supplementary Fig. 4) and its density-normalized log-transformation (Fig. 5a), indicating strong cooperativity as in Figs. 2b and 3h.

We extended Eq. 3 by assuming that increasing separation between TCR and CD4 would decrease the trimolecular bond formation exponentially, obtaining a phenomenological model that fits the data well:

$$\frac{\langle n \rangle_W}{m_{TCR}m_{pMHC}} = A_cK_{a,TCR}\left[1 + m_{CD4}K_{a,CD4}^* \exp\left(-\frac{x - x_0}{l}\right)\right] \quad (4)$$

where $A_cK_{a,TCR}$ ($1.29 \pm 0.52 \times 10^{-5}$ μm^4) was obtained from the TCR-alone measurement. Its smaller than other values in Table 1 may be explained by presenting TCR on different surfaces (RBCs vs origami-coated beads)[31]. Fitting returned an apparent separation x_0 (7.0 ± 1.7 nm) required for optimal cooperativity, decay length scale l (7.7 ± 2.1 nm), and CD4 affinity for TCR pre-engaged pMHC $K_{a,CD4}^*$ (0.050 ± 0.015 μm^2). The x_0 value agrees well with the 7-nm gap between the membrane anchors of TCR and CD4 found in their ternary structure complexed with pMHC[11], and values <7 nm lead to worse fits. The l value describes how fast the ability of CD4 to bind TCR-engaged pMHC would decay exponentially as x increases beyond x_0, underscoring the requirement for spatial proximity. The $K_{a,CD4}^*$ value is statistically indistinguishable from the value estimated from Fig. 2b using Eqs. 1 & 2 (Table 1).

To obtain independent support for the existence of trimolecular bonds, we analyzed single-bond stiffness to distinguish bimolecular vs trimolecular interactions[16] (Fig. 5b, c). When TCR and CD4 were spaced 20 or 100 nm apart, the histograms of molecular stiffness exhibited a single peak well fitted by a Gaussian distribution, yielding a mean stiffness of 0.32 pN/nm for both samples (Fig. 5c). Spacing the molecules 13 nm apart gave rise to a double-peak histogram (Fig. 5c). The first peak has nearly the same mean stiffness of 0.31 pN/nm but the second peak represents a subpopulation (38% of total) of nearly doubling the stiffness (0.58 pN/nm), indicating the presence of trimolecular bonds. The 6-nm spacing further populates the second peak (51%) but maintains the mean stiffness values for the two peaks (Fig. 5c). Interestingly, these fractions are consistent with the corresponding fractions with low and high average numbers of whole bonds ($\langle n \rangle_w$) normalized by the TCR and pMHC densities (m_{TCR} and m_{pMHC}) measured at 13 and 6 nm using the 2D assay (Fig. 5a). Overall, the data indicate that a threshold distance is required for TCR and CD4 to form trimolecular bonds with pMHC.

Discussion

A previous study using FRAP to analyze the mobility of TCR-CD3 or CD4 at the interface with pMHC observed reduced mobility of CD4 in
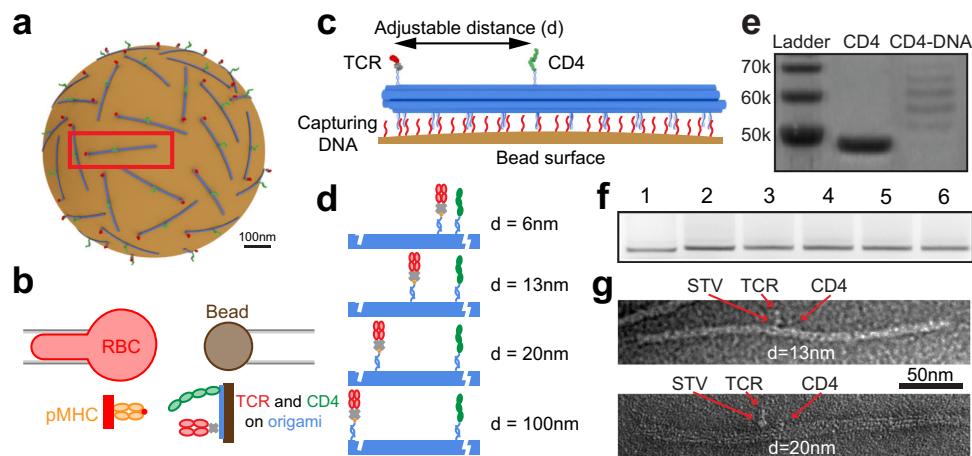
Fig. 4 | DNA origami-based platform for spacing control of TCR and CD4.
a Schematic of "surrogate" T cell – magnetic bead bearing 10 HB origami functionalized with precisely spaced TCR and CD4. **b** Schematic of micropipette adhesion frequency assay combined with ligand presentation by origami. **c** 10 HB origami controls separation distance of TCR and CD4 and attaches to magnetic bead via DNA strand hybridization. TCR binds to a streptavidin (SA), which also binds to a biotinylated DNA strand that hybridizes with a TCR-capturing DNA strand on 10HB origami. CD4 is covalently conjugated with a DNA stand that binds to a CD4-capturing strand. **d** Four distances were employed, with either 6, 13, 20, or 100 nm

TCR–CD4 spacing. **e** SDS PAGE of CD4 conjugated to oligonucleotide for loading onto 10HB origami. **f** Native agarose gel electrophoresis of 10 HB origami with (1) no poly-A extensions or protein handles, (2) poly-A extensions but no protein handles, 3-6 poly-A extensions with protein handles spaced at 6, 13, 20, and 100 nm respectively. **g** TEM image of 10HB origami bearing CD4 and SA-coupled TCR with 13 nm (top) and 20 nm (bottom) spacing. Experiments in **e** and **f** were repeated three times. TEM images in **g** are representative of 30-50 images collected from samples prepared in three separate experiments. Source data are provided as a Source Data file.

the presence of TCR–pMHC interaction and reduced TCR-CD3 mobility in the presence of CD4–MHC interaction[18], suggesting the binding of cellular TCR and CD4 to the same pMHC. Using two ultrasensitive mechanical assays to measure adhesion frequencies and single-bond lifetimes of three related 2D interaction systems – purified TCRαβ and CD4 ectodomains vs purified pMHC ectodomain, purified TCRαβ and CD4 ectodomains vs cellular pMHC, and cellular TCR-CD3 and CD4 vs purified pMHC ectodomain – and presenting the soluble proteins on the surface of RBCs, glass beads, and DNA origami, we showed in detail how and why this occurs despite the extremely low CD4–MHC affinity. By demonstrating that CD4 binds TCR-prebound pMHC with 3-6 logs (depending on the system) higher affinity than it binds free pMHC, our results explain how CD4 could efficiently augment TCR antigen recognition via stabilizing TCR–pMHC bonds and recruiting Lck to TCR-CD3. This also answered a perplexing question of why anti-CD4 blocking antibody would suppress Lck phosphorylation of CD3[32], if the CD4 could not even bind pMHC. While CD4 alone cannot initiate T cell interaction with APC, it is able to provide adequate "help" to TCR in recognition of cognate pMHC via enormous synergy and cooperation, a mechanism that greatly enhances TCR sensitivity.

Our work highlights the regulatory effects of force on dynamic cooperative molecular bonds. The cooperativity of mouse CD4 and TCR binding to Hb:I-E[k] could only be detected by the BFP force-clamp assay but not by the force-free adhesion frequency assay[10], suggesting that force on pMHC may enhance its on-rate for CD4. Our model also suggests that force-elicited catch bond enhances the sustainability of the pMHC-CD4 arm of the trimolecular bond by prolonging its lifetime.

An intriguing question raised by our findings is the molecular basis of the enhanced affinity of CD4 for TCR-prebound pMHC. The present work has ruled out the possibility that the TCR-CD4 cooperativity requires TCR–pMHC binding to induce inside-out signaling of CD4 to upregulate its affinity for pMHC, since soluble TCRαβ and CD4 proteins coated on RBC, glass bead, and DNA-origami surfaces are capable of cooperative binding to purified and cellular pMHC. Another possibility is that TCR binding to pMHC induces conformational changes in the CD4 binding site of MHC that increase affinity for CD4. However, crystallographic studies of numerous TCR and pMHC

molecules in free and bound form provide no evidence of TCR-induced structural changes at the site on the MHC class II β2 domain where CD4 binds. This would argue against an allosteric mechanism to explain increased CD4 affinity for TCR-prebound MHC. It is also possible that the relevant changes may be in protein dynamics, a parameter that cannot be addressed via the static snapshots provided by X-ray crystallography. Indeed, several NMR studies have found that pMHC binding to TCR induces long-range allosteric changes in TCR dynamics that could be relayed to CD3, even in the absence of obvious structural changes in the TCR[33–35]. The reverse situation (i.e. long-range allosteric changes in pMHC dynamics upon TCR binding) has not been examined by NMR, but probably should be given our results here.

The proposed structural mechanisms are supported by our modeling analysis, which was used to fit the bond lifetime data measured by the BFP experiments (Fig. 2d–f, Supplementary Fig. 3). To show this, we first compared the abilities of three models to simultaneously fit the three specific interaction data measured by thermal fluctuation (Fig. 2d). The first model is depicted in Supplementary Fig. 3a except that the activation to and dissociation from the strong state (TCR–pMHC)* is neglected because force was zero. Also, the weak (TCR–pMHC–CD4) and strong (TCR–pMHC–CD4)* trimolecular bonds are assumed to be in equilibrium and the two states dissociate concurrently to free molecules TCR + pMHC + CD4 in a single step (hence called concurrent model). The second model is a single-pathway, two-step, sequential dissociation model (sequential model I). It differs from the concurrent model in that the TCR–pMHC–CD4 trimolecular bond has only a single state that dissociates sequentially from right to left in Eq. 9 (Methods), first the pMHC–CD4 arm reversibly to generate TCR–pMHC complex + CD4, and then the TCR–pMHC bimolecular bond to free molecules TCR + pMHC + CD4. The third model is also a single-pathway, two-step, sequential dissociation model (sequential model II). It is similar to the sequential model I except that the order of sequential dissociation of the TCR–pMHC–CD4 trimolecular bond is reversed, which occurs first at the TCR–pMHC arm reversibly to generate pMHC–CD4 complex + TCR, and then at the pMHC–CD4 bimolecular bond to generate free molecules TCR + pMHC + CD4. Using the Akaike Information Criterion (AIC) to choose between two non-nested models, we found that the concurrent model is more likely to be
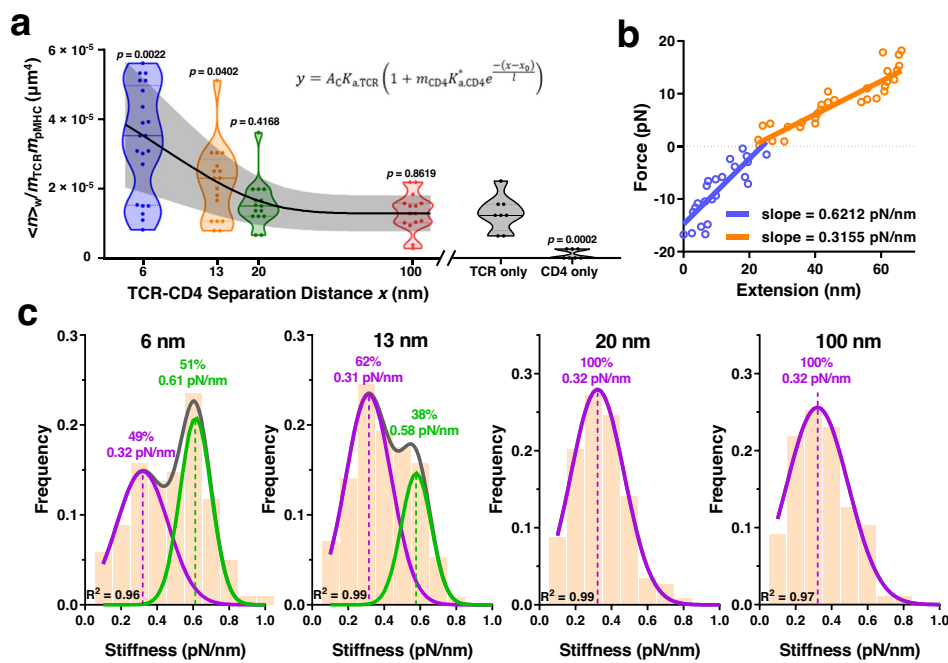
Fig. 5 | TCR-CD4 cooperativity is optimal at 7-nm spacing. a Normalized whole number of bonds $\langle n \rangle_w / m_{TCR} m_{pMHC}$ for pMHC-bearing RBCs interacting with DNA origami beads presenting TCR-CD4 pairs at 6, 13, 20, or 100 nm spacing, or presenting TCR alone or CD4 along (points, n = 21, 17, 15, 15, 8, and 7 cell-bead pairs). In the violin plots that show data densities, the solid lines in the middle represent mean and the lower and upper dotted lines represent the first and third quartiles. Equation 4 was fit (mean ± SE curves) to the $\langle n \rangle_w / m_{TCR} m_{pMHC}$ vs separation distance (x) data using the CD4 density (m_{CD4} = 31 μm^{-2}) measured by flow cytometry. *P*-values indicate comparison with TCR only group using two-tailed Mann-Whitney

test. **b** Representative force vs molecular extension plot illustrating the determination of molecular stiffness using the Hook's law. Blue: compression phase, where slope represents the spring constant of the cell. Orange: extension phase, where the slope represents the resultant spring constant of the cell the molecule connected in series. **c** Histograms of stiffness of bonds between pMHC and TCR and CD4 spaced at 6, 13, 20, or 100 nm. Histograms were fitted by single gaussian distribution (20 and 100 nm) or double gaussian distribution (6 and 13 nm) to identify the peak value(s) and the associated fractions. Source data are provided as a Source Data file.

correct than sequential model I by >58,000 times and even much more times than sequential model II. This conclusion still holds even when we analyzed data measured by force-clamp assay (Supplementary Fig. 3b) to evaluate their force-dependent kinetic parameters (Supplementary Fig. 3c, d). The concurrent model suggests a strong functional coupling between the spatially separate TCR binding site and the CD4 binding site on the pMHC, supporting our allostery hypothesis. Future studies are required to test this hypothesis. Moreover, to confirm that association and dissociation happen preferentially via pathway I instead of pathway II, we considered a more general two-pathway, two-step model that combines both sequential models I and II, and globally fit the adhesion frequency data from Fig. 2a, b. We compared it to the sequential model I by AIC, and found little difference statistically, suggesting that both association and dissociation along the first pathway (i.e., sequential model I) dominates over the second pathway (i.e., sequential model II), which only happens with very low probability (~0.99 and ~0.01 for pathway I and II, respectively, of the two-pathway, two-step model).

This work builds upon our previous findings of TCR-CD8 cooperativity for class-I pMHC binding[6,13–16] and adds to our previously proposed mechanistic model[16,36]. In live-cell systems, cooperativity relies on the recruitment of coreceptor to phosphorylated CD3 via a Lck "bridge", where both the adaptor function and kinase function of Lck are required[13,14,16,36,37] as seen with co-immunoprecipitation studies that identify similar molecular assembly connecting CD4 or CD8 to triggered TCR-CD3[3,38–41]. Here we show that using purified TCR and CD4 lacking cytoplasmic domains and CD3, the synergistic cooperation could still occur if both molecules are allowed to diffuse on the RBCs or packed closed enough on the bead surface, suggesting that modulation of ectodomain cooperation could be decoupled from intracellular regulation. This is also consistent with the observation

that CD4 lacking the ability of binding Lck is still required for TCR-mediated IL-2 production[18]. On the other hand, our data of cellular TCR and CD4 cooperating with a faster kinetics than their purified ectodomain counterparts regardless of being tested against purified pMHC or cellular pMHC suggest that there may be cellular regulation(s) to expedite TCR-CD4 cooperativity. Modulation of ectodomain by physical factors such as mobility and colocalization are intuitive, but require 2D analyses to decipher. Indeed, by limiting mobility using different surface and controlling TCR-CD4 proximity using DNA origami, we found a 7-nm apparent spacing for TCR-CD4 cooperativity, such that increasing the spacing resulted in an exponential decay in the capacity to form TCR−pMHC−CD4 trimolecular bonds. Such physical regulatory mechanisms revealed by the in vitro system further advance our understanding of how interactions between membrane receptors and ligands critically depend on their cell surface organization. Methodologically, our DNA origami-based 2D kinetic assays hold great potential to dissect the spatial requirement of the cooperation of single- or multi-receptor−ligand species by ectodomain binding and/or intracellular crosstalk.

Methods

All experiments in this study were conducted with the compliance to the Institutional Review Board of Georgia Institute of Technology.

Proteins

Biotinylated CD4 and biotinylated αβ E8 TCR were prepared as previously described[7,21]. Briefly, a 17-amino acid tag (TPI, GGGLNDI-FEAQKIEWHE) was added to the C-terminus of CD4 ectodomain and to the C-terminus of the E8 TCRα ectodomain. CD4 was expressed in baculovirus-infected Sf9 insect cells[7]. E8 TCR was produced by in vitro folding from inclusion bodies expressed in *E. coli*[21]. The purified

proteins were biotinylated using biotin protein ligase (Avidity); excess biotin and ligase were removed with a Superdex 200 column (GE Healthcare). The control MHC-I (HLA-A2) presenting the melanoma antigen peptide NY-ESO-1$_{157-165}$ (9V, SLLMWITQV) was produced by the NIH Tetramer Facility at Emory University.

Biotinylated TPI: HLA-DR1 was made by the NIH Tetramer Core facility (Atlanta, GA) with peptide (GELIGTLNAAKVPAD) purchased from GenScript. Divalent streptavidin was generously gifted by Dr. Baoyu Liu (University of Utah).

Cells

Human RBCs were isolated from blood of healthy donors according to a protocol approved by the Institutional Review Board of Georgia Institute of Technology with informed consent from the donor. For adhesion frequency assay, RBCs were purified by Histopaque-1077, washed with ice-cold PBS, and resuspended in EAS-45 buffer (2 mM Adenine, 110 mM D-glucose, 55 mM D-Mannitol, 50 mM Sodium Chloride, 20 mM Sodium Phosphate, and 10 mM L-glutamine). Equal aliquots of RBCs were then mixed with various concentrations of EZ-Link Sulfo-NHS-LC-Biotin (Thermo Scientific) at a pH of 7.2 for 30 min at room temperature, yielding different densities of biotin sites on RBC surfaces. Biotinylated RBCs were washed with EAS-45 buffer and stored at 4 °C. For BFP experiments, freshly isolated human RBCs were biotinylated with biotin-PEG3500-NHS (Jenkem Technology) and then incubated with nystatin in N2 buffer (265.2 mM KCl, 38.8 mM NaCl, 0.94 mM KH2PO4, 4.74 mM Na2HPO4, and 27 mM sucrose; pH 7.2 at 588 mOsm) for 30 min on ice. Nystatin-treated biotinylated RBCs were washed twice with N2 buffer and stored at 4 °C for BFP experiments.

HEK 293 T cells were purchased from ATCC (Manassas, VA) and cultured in DMEM supplemented with 10% FBS, 6 mM L-glutamine, 0.1 mM MEM non-essential amino acids, and 1 mM sodium pyruvate. TCR β-chain deficient Jurkat J.RT3 cells were purchased from ATCC (Manassas, VA) and cultured in RPMI 1640 supplemented with 10% FBS, 100 U/mL penicillin, 100 μg/mL streptomycin, 2 mM L-glutamine, and 20 mM HEPES. J.RT3 were transduced by lentivirus to express the E8 TCR. Briefly, E8 TCR α and β chains joined by a P2A element were subcloned into pLenti6.3 vector with a T2A-rat CD2 reporter. Lentivirus encoding E8 TCR were produced by co-transfection of HEK 293 T cells with E8TCR-pLenti6.3, pMD2.G (Addgene #12259), and psPAX2 (Addgene #12260) using lipofectamine 3000 (ThermoFisher Scientific). J.RT3 cells were transduced by incubating overnight with supernatant containing lentivirus and FACS sorted using Aria cell sorter (BD Biosciences) based on the surface expression E8 TCR. E8TCR J.RT3 cells were then transfected using Nucleofection (Lonza, Morristown, NJ) to express full-length human CD4 and FACS sorted using Aria cell sorter (BD Biosciences) for stable CD4 expression. THP-1 cells were cultured in RPMI 1640 supplemented with 10% FBS, 100 U/mL penicillin, 100 μg/mL streptomycin, 2 mM L-glutamine, and 20 mM HEPES. One day prior to experiment, the cells were treated with 20–100 U/ml IFN-γ (R&D Systems) and 1 μM TPI peptide (Genscript).

Site density measurements

Site densities of TCR, CD4, and pMHC on RBCs, Jurkat cells, THP-1 cells, glass beads, or origami beads were measured by flow cytometry using PE-conjugated antibodies from BD Biosciences (San Jose, CA): anti-human TCR-β1 (clone JOVI.1, 1:20), anti-human CD4 (clone OKT4, 1:20), and anti-human HLA-DR (clone L243, 1:5). Isotype control antibodies were PE mouse IgG2a κ (clone G155-178, 1:20) for TCR and HLA-DR, and PE mouse IgG2b, κ (Clone 27-35, 1:20) for CD4. RBCs or beads were incubated with corresponding antibodies in 1X PBS + 2% BSA for 30 min at 25 °C and washed three times before being analyzed using the BD Accuri or Fortessa Flow Cytometer. Data were collected with FACSDiva v9 and analyzed with Flowjo v10. An example of gating strategy is shown in Supplementary Figure 5. Site density was calculated based on antibody-conjugated PE fluorescence relative to the QuantiBRITE PE standard beads (BD Biosciences). For micropipette experiments, RBCs bearing protein of interest (TCR, CD4, or MHC) were prepared for flow cytometry using three separate samples: one saturating the RBC surface, one of the experimental conditions, and one isotype control. Brightness across all antibodies was normalized against the CD4 staining which was brighter than the TCR staining.

Micropipette Adhesion Frequency Assay

The theoretical framework and detailed experimental procedures of this assay have been described previously[19,20,42]. This assay leverages the ultra-soft RBC membrane to detect interactions with single-bond sensitivity. Briefly, RBCs with controlled biotin sites were first incubated with 200 μg/mL divalent streptavidin and washed, followed by subsequent coating with biotinylated pMHC, TCR, CD4, or a mixture of TCR and CD4. After washing, RBCs coated with receptor-ligand pairs were injected into an imaging chamber containing non-CO2 dependent L15 media supplemented with HEPES and 2% BSA. During experiment, two RBCs were aspirated by micropipette and repeatedly brought into contact of defined duration by a program-controlled piezo. Adhesion between two RBCs were detected by the deflection of RBC membrane during the separation after each contact with '1' indicating an adhesive event and '0' indicating no adhesion. Each pair of RBCs were tested for 50 cycles of the same contact duration to yield the adhesion frequency (P_a), which is as the average score from the 50 cycles. The same process was repeated for multiple pairs of RBC of each contact duration (t_c), yielding a P_a vs t_c curve that is fitted to a published model[19,20] (see below).

Non-specific controls were conducted for all sets of species coatings. To do so, RBCs coated with divalent streptavidin anchored irrelevant protein (OT1 TCR) were brought into contact with RBCs coated with proteins of interest. An adhesion frequency curve would be obtained for nonspecific adhesion. Then, for each contact time, the distribution of nonspecific adhesion frequency would be removed from the measured distribution of adhesion frequency[23–25].

In some experiments, one or both sides of the RBCs were replaced by glass beads coated with pMHC (see below) or THP-1 cells expressing pMHC, or glass beads or origami beads coated with TCR, CD4, or both (see below), or expressed on Jurkat cells expressing TCR, CD4, or both. Data collection with precise pizeo movement control was using Labview 2016&2019 and Excel 2016.

Biomembrane Force Probe Assay

The principle and experimental procedures for BFP assays have been described previously[27]. To coat proteins on beads, borosilicate glass beads were mercapto-propyl silanated and covalently functionalized to monovalent streptavidin-maleimide in phosphate buffer saline (pH 6.8) by overnight incubation at 25 °C. Streptavidinylated beads were then incubated with sub-saturating concentrations of biotinylated pMHC, TCR, CD4, or 1:1 mixture of TCR and CD4 for 2 h in HBSS + 2% BSA at 4 °C. For CD4 blocking, T cells were treated with antiCD4 (GK1.5, 1:10) for 30 min and analyzed with the presence of antiCD4 in the chamber. During the experiment, a protein-coated bead (tracking bead) was attached to the apex of a micropipette-aspirated RBC that serves as a spring with pre-adjusted spring constant of 0.1-0.3 pN/nm. For force clamp assay, the tracking bead was repeatedly contacted by a piezo-driven target bead coated with (or target cell expressing) the corresponding binding partner(s). The displacement of tracking bead was monitored with a high-speed camera at 1000 fps and was translated into force by applying the pre-defined spring constant. During separation, bond formation between tracking bead and target bead/cell pulled the tracking bead away from its baseline, manifesting positive force loading on the molecular bond. Bond lifetime was defined as the duration from the start of clamp at the preset force level to bond rupture. Several hundred bond lifetime events were collected

and pooled for various clamp forces using multiple bead-bead or bead-cell pairs. The stiffnesses of molecular bonds were modeled as Hookean spring constants which is determined by the difference between the displacements of the bead tracking system (F) and the displacements of the piezoelectric actuator-capacitance sensor feedback system (Δx). Two straight lines were fitted to the piecewise data: One was fitted to the compressive force regime where the bead was slowly ramping away from cell impingement (force <0), where the slop represents the spring constant of the cell membrane (compression). The other was fitted to the tensile force regime where the bead would ramp away from the cell beyond the point of initial contact (force >0), where the slop represents the resultant spring constant of cell membrane (extension) and molecular bond connected in series. By assuming the spring constant of cell membrane is identical during compression as during extension, the spring constant of molecular bond was extracted by applying Hooke's law for springs in series. An ensemble of molecular spring constant was collected as histograms using similar force bins and fitted to single or double Gaussian distributions.

For thermal fluctuation assays[20,26], a target bead was driven by piezo to the proximity (-10 nm) of the probe bead, allowing bond formation between the two during intermittent contacts caused by thermal fluctuation, which would decrease the fluctuation of probe bead position. By analyzing the standard deviation (SD) of the tracking bead position, bond formation and rupture were identified by the decrease of SD below a cutoff of 3 nm and the subsequent resumption SD to baseline level. The cutoff baseline was determined as the lowest SD value of the probe bead before contact (*i.e.*, SD of bead without bonds).

For adhesion frequency assays using BFP beads, the same process of RBC-based adhesion frequency assay was performed except that a target cell was repeatedly brought into contact with a pMHC-coated bead, held for a defined duration, and then separated. Adhesion was defined as the deflection of bead away from its equilibrium position.

Kinetic models
Single-step model for bimolecular interaction.
The bimolecular interactions of either TCR or CD4 with pMHC are modeled as a single-step reversible reaction:

$$R+L \underset{k_{-1}}{\overset{k_{+1}}{\rightleftharpoons}} B \qquad (5)$$

where R, L, and B denote, respectively, receptor, ligand, and bond; k_{+1} and k_{-1} denote, respectively, on- and off-rates. Their ratio is the binding affinity, $K_a = k_{+1}/k_{-1}$. Our published probabilistic kinetic model for the above reaction states that the probability of adhesion (P_a) depends on the contact time (t_c) and area (A_c) as well as the densities of receptors (m_r) and ligands (m_l)[19,20].

$$P_a = 1 - \exp\{-m_r m_l A_c K_a [1 - \exp(-k_{-1}t_c)]\} \qquad (6)$$

On the right-hand side, the term inside the braces after the minus sign is the average number of bonds per contact <n>.
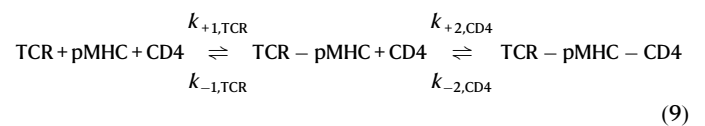
$$\langle n \rangle = m_r m_l A_c K_a [1 - \exp(-k_{-1}t_c)] \qquad (7)$$

After normalizing <n> by $m_r m_l$, the right-hand should be independent of the molecular densities and approaches $A_c K_a$, the effective 2D affinity, as t_c becomes large.

$$\frac{\langle n \rangle}{m_r m_l} = A_c K_a [1 - \exp(-k_{-1}t_c)] \rightarrow A_c K_a \quad \text{as } t_c \gg 1/k_{-1} \qquad (8)$$

It follows from Eq. 8 that <n>is proportional to $m_r m_l$ if measured at large contact time.

We use TCR or CD4 in the subscript to identify the interaction with which the kinetic parameters are associated, e.g., $k_{+1,TCR}$, $k_{-1,TCR}$, and $K_{a,TCR}$ are kinetic rates and binding affinity for the TCR−pMHC interaction, which are different from $k_{+1,CD4}$, $k_{-1,CD4}$, and $K_{a,CD4}$, which are corresponding parameters for the CD4−MHC interaction. Also, m_{TCR}, m_{CD4}, and m_{pMHC} are used to designate the densities of TCR, CD4, and pMHC.

Two-step model for trimolecular interaction.
We propose a two-step model for the formation of trimolecular bonds. Since the affinity and on-rate for the CD4−pMHC interaction are so much smaller than those of the TCR−pMHC interaction, it seems reasonable to assume that TCR interacts with pMHC at the same kinetic rates as bimolecular interaction in the first step as if CD4 does not interact with free pMHC. However, CD4 is able to interact with TCR-stabilized pMHC with a much higher affinity, thereby forming trimolecular bonds in the second step.

$$\text{TCR} + \text{pMHC} + \text{CD4} \underset{k_{-1,TCR}}{\overset{k_{+1,TCR}}{\rightleftharpoons}} \text{TCR} - \text{pMHC} + \text{CD4} \underset{k_{-2,CD4}}{\overset{k_{+2,CD4}}{\rightleftharpoons}} \text{TCR} - \text{pMHC} - \text{CD4}$$
$$(9)$$

Let $p_{m,n}$ be the probability of having m TCR−pMHC bonds and n TCR−pMHC−CD4 bonds, which are governed by the following master equations:

$$\frac{dp_{m,n}}{dt} = m_{TCR}m_{pMHC}A_c k_{+1,TCR}p_{m-1,n} + k_{-1,TCR}(m+1)p_{m+1,n}$$
$$+ m_{CD4}k_{+2,CD4}(m+1)p_{m+1,n-1} + k_{-2,CD4}(n+1)p_{m-1,n+1}$$
$$- [m_{TCR}m_{pMHC}A_c k_{+1,TCR} + (k_{-1,TCR} + m_{CD4}k_{+2,CD4})m + k_{-2,CD4}n]p_{m,n}$$
$$(10)$$

We solved these master equations using a probability generating function,

$$g(x,y;t) \equiv \sum_{m,n=0}^{\infty} x^m y^n p_{m,n}(t), \qquad (11)$$

which converts Eq. 10 to a single first-order linear partial differential equation,

$$\frac{\partial g}{\partial t} + \left[(k_{-1,TCR} + m_{CD4}k_{+2,CD4})x - m_{CD4}k_{+2,CD4}y - k_{-1,TCR} \right] \frac{\partial g}{\partial x}$$
$$+ k_{-2,CD4}(y-x)\frac{\partial g}{\partial y} + m_{TCR}m_{pMHC}A_c k_{+1,TCR}(1-x)g = 0. \qquad (12)$$

We found a general solution to Eq. 12 using the method of characteristics, which is

$$g = J\left(u_1 e^{-\lambda_1 t}, u_2 e^{-\lambda_2 t}\right)\exp\{m_{TCR}m_{pMHC}A_c K_{a,TCR}[x - y + (1 + m_{CD4}K^*_{a,CD4})(y-1)]\} \qquad (13)$$

where J is an arbitrary function of its two arguments. u_1 and u_2 are functions of x and y:

$$u_{1,2}(x,y) = \pm [\lambda_{2,1}(1-y) + k_{-2,CD4}(y-x)]/(\lambda_1 - \lambda_2), \qquad (14)$$

λ_1 and λ_2 are given by Eq. 2. They can be viewed as the fast (λ_1) and slow (λ_2) rates that control the two p44hases of the two-step interaction. To determine the function of integration J requires initial conditions. If there is no TCR−pMHC or TCR−pMHC−CD4 bonds at $t=0$, the initial conditions on $p_{m,n}$ are:

$$p_{m,n}(0) = \begin{cases} 1, & m=n=0 \\ 0, & m,n > 0 \end{cases}. \qquad (15)$$

The corresponding initial condition of g, obtained by substituting Eq. 15 into Eq. 11, is

$$g_{00}(x,y;0) = 1. \qquad (16)$$

Solving x and y in terms of $u_{1,2}$ from Eq. 14, substituting them into Eq. 16, and comparing the resulting equation to Eq. 13 evaluated at $t = 0$ allows us to solve for a particular solution for J:

$$J_{00}(u_1,u_2) = \exp\{m_{TCR}m_{pMHC}A_c K_{a,TCR}[(\lambda_1/k_{-2,CD4})u_1 \\ + (\lambda_2/k_{-2,CD4})u_2 - (1 + m_{CD4}K^*_{a,CD4})(u_1 + u_2)]\}. \qquad (17)$$

Substituting Eq. 17 into Eq. 13, we have

$$g_{00}(x,y;t) = \exp\Bigg(m_{TCR}m_{pMHC}A_c K_{a,TCR}\Bigg\{ k_{-1,TCR}\left(\frac{e^{-\lambda_1 t} - e^{-\lambda_2 t}}{\lambda_1 - \lambda_2}\right) \\ - \left(1 + m_{CD4}K^*_{a,CD4}\right)\left(1 + \frac{\lambda_2 e^{-\lambda_1 t} - \lambda_1 e^{-\lambda_2 t}}{\lambda_1 - \lambda_2}\right) \\ + \left[1 + \frac{(\lambda_2 - k_{-1,TCR})e^{-\lambda_1 t} - (\lambda_1 - k_{-1,TCR})e^{-\lambda_2 t}}{\lambda_1 - \lambda_2}\right]x \\ + m_{CD4}K^*_{a,CD4}\left(1 + \left(\frac{\lambda_2 e^{-\lambda_1 t} - \lambda_1 e^{-\lambda_2 t}}{\lambda_1 - \lambda_2}\right)y\right)\Bigg\}\Bigg) \qquad (18)$$

Expanding the right-hand side of Eq. 18 into Taylor series of x and y, and comparing the coefficients of the $x^m y^n$ terms to those of the right-hand side of Eq. 11, we found

$$p_{m,n}(t) = \left[\frac{\langle m\rangle^m}{m!}\exp(-\langle m\rangle)\right]\left[\frac{\langle n\rangle^n}{n!}\exp(-\langle n\rangle)\right] \qquad (19a)$$

where

$$\langle m\rangle = \langle n\rangle_{TCR} = m_{TCR}m_{pMHC}A_c K_{a,TCR}\left[1 + \frac{(\lambda_2 - k_{-1,TCR})e^{-\lambda_1 t} - (\lambda_1 - k_{-1,TCR})e^{-\lambda_2 t}}{\lambda_1 - \lambda_2}\right] \qquad (19b)$$

$$\langle n\rangle = \langle n\rangle_{tri} = m_{TCR}m_{pMHC}A_c K_{a,TCR}m_{CD4}K^*_{a,CD4}\left(1 + \frac{\lambda_2 e^{-\lambda_1 t} - \lambda_1 e^{-\lambda_2 t}}{\lambda_1 - \lambda_2}\right) \qquad (19c)$$

are the average numbers of TCR–pMHC bonds and TCR–pMHC–CD4 bonds. Thus, the solution is of the form of the product of two Poisson distributions. Except for the expressions for <m> and <n>, this is the same as the bond distribution of the dual species concurrent independent binding model described previously[23–25].

The adhesion probability is the probability of having at least one bond of either type, or one minus the probability of having no bond, which can be found from Eq. 19:

$$P_a(t) = 1 - \exp\Bigg\{ -m_{TCR}m_{pMHC}A_c K_{a,TCR}\left(1 + m_{CD4}K^*_{a,CD4}\right) \\ \times \left[1 + \frac{\lambda_2(\lambda_2 - k_{-1,TCR})e^{-\lambda_1 t} - \lambda_1(\lambda_1 - k_{-1,TCR})e^{-\lambda_2 t}}{(\lambda_1 - \lambda_2)(m_{CD4}k_{+2,CD4} + k_{-2,CD4})}\right]\Bigg\} \qquad (20)$$

Taking a log transformation, we obtain the average number of whole bonds $\langle n\rangle_W = -\ln(1 - P_a)$. Normalizing $\langle n\rangle_W$ by the densities of TCR and pMHC, we obtain Eq. 1. Setting $k_{+2,CD4} = k_{-2,CD4} = 0$ reduces Eq. 2 to $\lambda_1 = k_{-1}$ and $\lambda_2 = 0$, which also reduces Eqs. 20 and 1 to Eqs. 6 and 8, respectively, as expected.

DNA Origami preparation
Origami were created at 20 nM using p8064 scaffold, 5× staple excess, and 25× biotin strand for TCR capture. Following agarose gel

electrophoresis in 1% agarose at 60 V for 90 min on ice bath, origami were purified with Freeze 'n' Squeeze spin columns. The four samples with different protein separation distances were indistinguishable based on gel mobility. However, a control sample with only handles for surrogate cell attachment ran with slightly increased mobility, while a complete blank 10 HB sample with no handle extensions whatsoever ran markedly faster through the gel. To confirm proper assembly of protein onto the DNA origami, purified samples were incubated with excesses of CD4–DNA and wild type streptavidin at 4 °C overnight. After another agarose gel purification, a 10-fold molar excess of biotinylated TCR was added and allowed to incubate at 4 °C for 3 h. Excess protein was removed using 100 kD MWCO spin filters, then the samples were deposited on 400 mesh carbon formvar grids and stained with 1% uranyl formate solution for 30 s. During TEM imaging, the identity of blinded samples could be reliably divined by observing relative CD4, SA–TCR location.

An amine-modified DNA strand was conjugated to lysine residues in CD4. CD4 was reacted with 50-fold excess succinimidyl-6-hydrazino-nicotinamide (S-HyNic) (Solulink) for 4 h, and terminal amine DNA was reacted with 20-fold excess succinimidyl-4-formylbenzene (S-4FB) (Solulink) for 4 h. Amicon Ultra spin filters (Millipore) were used to remove excess linker and buffer exchange into citrate buffer (50 nM sodium citrate, 150 mM NaCl, pH 6). Functionalized DNA was combined with CD4 at a 3:1 ratio, and reacted overnight. CD4-DNA conjugates were purified on a Superdex 200 Increase 10/300 GL column using an AKTA Pure FPLC (GE Healthcare). Conjugation was verified with SDS/PAGE and Coomassie blue staining.

In order to examine the effect of geometric docking on the simultaneous interaction of two molecules with a third, origami structures differentially spacing TCR and CD4 were coated on beads to represent a simplified T cell surface. Beads were respectively coated with several different origami structures: those with handles for TCR and CD4 which were differentially spaced apart at 6, 13, 20, and 100 nm; those lacking protein handles; and origami lacking connecting strands to the beads. The purified samples were loaded onto surrogate T cells –3 µm diameter magnetic dt Dynabeads. For each sample, 15 µL of beads were washed 3× with PBS then added to 1 µg (-30 µL) of purified DNA origami. A large excess of CD4–DNA and streptavidin were added, and the samples were left to incubate on a rotating shaker at 4 °C overnight. The magnetically pelleted beads were washed with PBS supplemented with calcium and magnesium, and 2% BSA five times. Biotinylated (at the C-terminus of the α-chain) E8 TCR was added to the beads and incubated for 30 min. To this solution, blocking DNA strand (25 dA) was added and the reaction incubated at 4 °C for an additional 1 h.

Fitting models to data
Linear fittings of data in Fig. 2d, Fig. 5b, Supplementary Fig. 1, and Supplementary Fig. 2c were implemented in Prism using linear regression to estimate the slope and y-intercept of the trend. Non-linear fittings of bimolecular kinetic equations to data in Fig. 1c,d were implemented in Prism using Non-linear regression to estimate the corresponding kinetic parameters. Gaussian fitting of data in Fig. 5c was implemented in Prism using non-linear regression to estimate the Gaussian distribution and frequency of each distribution. For all fitted parameters, fitting error was presented as Standard Error (SE) assuming symmetrical confidence intervals.

The model predicted curves in Fig. 2a–c and Supplementary Fig. 2a were obtained by globally fitting all data to Eqs. 1 & 2, which were also fit to data in Fig. 3a, b, d, e, h. For the Fig. 3h case, the green and black data were globally fit, the orange data was fit on its own, and the blue data was fit after constraining the off-rates obtained from the orange data fit to avoid overfitting. Best-fit Pa ± SE (curves) in Fig. 3a was calculated from best-fit <n> ± SE in Fig. 3b. p = 0.0563, 0.0159, 0.0631, 0.1200, 0.0502, and 0.0405 for comparing measured Pa of

whole interactions to predicted sum at tc = 0.5, 1, 2, 4, 8, and 16 s calculated from one-tailed t-test independently for each contact time. In Fig. 3b, predications were made after normalizing the densities in different curves. TCR + CD4 curve was fitted while keeping the same TCR affinity and off-rate as in the bimolecular interaction. p = 0.0552, 0.0162, 0.0624, 0.1179, 0.0523, and 0.0473 for comparing measured whole bonds to predicted sum at tc = 0.5, 1, 2, 4, 8, and 16 s calculated from one-tailed t-test independently for each contact time. Best-fit Pa ± SE in Fig. 3d was calculated from best-fit <n> ± SE in Fig. 3e. p = 0.0016, 0.0004, 0.0013, 0.00005, 0.0004, and 0.0066 for comparing measured Pa of whole interactions to predicted sum at tc = 0.5, 1, 2, 4, 8, and 16 s calculated from one-tailed t-test independently for each contact time. In Fig. 3e, p = 0.0022, 0.0006, 0.0019, 0.0001, 0.0011, and 0.0140 for comparing measured whole bonds to predicted sum at tc = 0.5, 1, 2, 4, 8, and 16 s calculated from one-tailed t-test independently for each contact time. p = 0.0044, 0.0013, 0.0066, 0.0029, 0.3089, and 0.5179 for comparing measured whole bonds to its fitted curve (brown) at tc = 0.5, 1, 2, 4, 8, and 16 s calculated from one-tailed t-test independently for each contact time.

The separation distance-dependent adhesion frequency of the DNA origami assay (Fig. 5a) was fit to Eq. 4. For Figs. 2a–c, 3a, b, d, e, h, a two-step optimization procedure was employed to minimize the mean squared error (MSE) of the fits with respect to the data, which explored a large parameter space by Differential Evolution to obtain an approximate solution, followed by L-BFGS to hone in the minimum. The parameters Standard Errors (SE) were calculated from the covariance matrix obtained by inverting the Hessian matrix of the loss function at the minimum found. The SEs were then propagated through the model to display error bands of the fits as mean ± SE. The data in Fig. 5a were also fitted by the aforementioned two-step optimization procedure but the parameters SE were obtained via bootstrapping, with 1000 bootstrap samples.

The force-dependent lifetimes of pMHC bonds with TCR alone or co-presented TCR and CD4 behaved as catch-slip bonds, while pMHC bonds with CD4 alone behaved as a slip bond. Although at zero force the two catch-slip bonds had mono-exponentially decaying survival probabilities (Fig. 2d), a second population appeared at forces >0, displaying biexponentially decaying survival probabilities, suggesting the presence of two bound species, even for the bimolecular TCR–pMHC. Therefore, while the CD4–pMHC bonds were modelled to dissociate along a single pathway, both TCR–pMHC and TCR–pMHC–CD4 bonds were modelled to dissociate along two pathways – a fast dissociating pathway from a weak state or a slow dissociating pathway from a strong state (indicated by *) allowed to exchange from each other as depicted in Supplementary Fig. 3a (left and right panels) similarly to previous catch bond models[43,44]. The force dependence of all kinetic rates follows Bell's equation[45]:

$$k_{i,j}(f) = k_{i,j}^0 \exp\left(\frac{f \cdot x_{i,j}}{k_B T}\right) \tag{21}$$

where f is force, the superscript 0 denotes the zero-force kinetic rate constant, the subscript i denotes rates of dissociation along fast (-f) or slow (-s) pathways and of activation (-a) or deactivation (-a) transition between the weak and strong states, the subscript j denotes different bonds (TCR–pMHC or TCR–pMHC–CD4), $x_{i,j}$ denotes distance to the transition state, or width of the energy well that traps the system in the bound state, k_B is Boltzmann constant, and T is absolute temperature. The weak state dissociates more rapidly than the strong state, so $k_{-f,i} > k_{-s,i}$. The two-states, two-path catch-slip model can be expressed in terms of ordinary differential equations that govern the probability of

having bonds P at a given time t:

$$\begin{cases} \frac{dP_j}{dt} = -k_{-f}P_j - k_a P_j + k_{-a}P_{(j)^*} \\ \frac{dP_{(j)^*}}{dt} = -k_{-s}P_{(j)^*} + k_a P_j - k_{-a}P_{(j)^*} \end{cases} \tag{22}$$

where the subscript j, as above, stands for TCR–pMHC or TCR–pMHC–CD4 bonds in the weak (without *) or strong (with *) state, and all rates k_i vary as a function of force as given by Eq. 21. This two-state catch-bond model could recapitulate the average bond lifetime as well as the biexponentially distributed bond survival probabilities of both TCR–pMHC and TCR–pMHC–CD4 interactions. All kinetic parameters were determined by globally fitting the models to the force-lifetime distributions as a whole via maximum likelihood estimation (MLE). The initial proportions of the two states a $t = 0$ were determined from the ratios of the kinetic rates assuming equilibrium. A two-step optimization procedure was employed to minimize the MLE, which explored a large parameter space by Differential Evolution to obtain an approximate solution, followed by L-BFGS to home in the minimum. This returns the best-fit parameters summarized in Supplementary Fig. 3d. The force dependence of the kinetic rates is graphically depicted in Supplementary Fig. 3c. Using Eqs. 21 & 22 with the best-fit parameters we calculated the probability of the strong state and its fraction as functions of time and force for both TCR–pMHC and TCR–pMHC–CD4 interactions (Supplementary Fig. 3e–f). The same equations and best-fit parameters predict the mean ± SE of lifetime vs force of the TCR–pMHC, pMHC–CD4 and TCR–pMHC–CD4 bonds that agree well with the mean ± SEM data of these interactions (Fig. 2e). Also predicted are the average lifetime vs force of weak state, strong state, and their sum of the trimolecular bond that shows the force enhancement of cooperativity (Fig. 2f). It is important to note that although the two-state, two-path model fits the data as a catch-slip bond, this does not need to always be the case. In fact, the two-state, two-path model could in theory also yield slip bond or slip-catch-slip bond behavior given specific sets of parameters. Nevertheless, the catch-slip behavior naturally arises from maximizing the likelihood of the TCR–pMHC and TCR–pMHC–CD4 force-lifetime distributions, in good agreement with the average lifetimes of each bin obtained independently from the fitting. This further adds confidence both in the existence of the two catch-bonds as well as the reliability of the model. The standard error for each parameter was obtained by inverting the Hessian matrix of the negative log-likelihood at the MLE to obtain the approximate covariance matrix whose diagonal entries correspond to the variance of the fitted parameters. All kinetic modeling and associated statistics were programmatically implemented in Matlab 2020a, Julia 1.6, and Python 3.7.

Reporting summary

Further information on research design is available in the Nature Portfolio Reporting Summary linked to this article.

Data availability

Data supporting the findings of this study are presented in the article and supplementary materials and are available from the corresponding authors upon reasonable request. Source data are provided with this paper.

Code availability

The code used to fit the data presented in this study is available at https://github.com/vaglino/TCR-MHC-CD4_kinetic_modeling under MIT license.

References

1. Courtney, A. H., Lo, W. L. & Weiss, A. TCR Signaling: Mechanisms of Initiation and Propagation. *Trends Biochem. Sci.* **43**, 108–123 (2018).

2. Rudd, C. E. CD4, CD8 and the TCR-CD3 complex: a novel class of protein-tyrosine kinase receptor. *Immunol. Today* **11**, 400–406 (1990).

3. Xu, H. & Littman, D. R. A kinase-independent function of Lck in potentiating antigen-specific T cell activation. *Cell* **74**, 633–643 (1993).

4. Mørch, A. M., Bálint, Š., Santos, A. M., Davis, S. J. & Dustin, M. L. Coreceptors and TCR Signaling—the Strong and the Weak of It. *Front. Cell Dev. Biol.* **8**, 597627 (2020).

5. Glatzova, D. & Cebecauer, M. Dual role of CD4 in peripheral T Lymphocytes. *Front. Immunol.* **10**, 618 (2019).

6. Jonsson, P. et al. Remarkably low affinity of CD4/peptide-major histocompatibility complex class II protein interactions. *Proc. Natl Acad. Sci. USA* **113**, 5682–5687 (2016).

7. Wang, X. X. et al. Affinity maturation of human CD4 by yeast surface display and crystal structure of a CD4-HLA-DR1 complex. *Proc. Natl Acad. Sci. USA* **108**, 15960–15965 (2011).

8. Xiong, Y., Kern, P., Chang, H. & Reinherz, E. T cell receptor binding to a pMHCII ligand is kinetically distinct from and independent of CD4. *J. Biol. Chem.* **276**, 5659–5667 (2001).

9. Huppa, J. B. et al. TCR-peptide-MHC interactions in situ show accelerated kinetics and increased affinity. *Nature* **463**, 963–967 (2010).

10. Hong, J. et al. Force-regulated in situ TCR-peptide-bound MHC Class II kinetics determine functions of CD4+ T cells. *J. Immunol.* **195**, 3557–3564 (2015).

11. Yin, Y., Wang, X. X. & Mariuzza, R. A. Crystal structure of a complete ternary complex of T-cell receptor, peptide-MHC, and CD4. *Proc. Natl Acad. Sci.* **109**, 5405–5410 (2012).

12. Dong, D. et al. Structural basis of assembly of the human T cell receptor-CD3 complex. *Nature* **573**, 546–552 (2019).

13. Jiang, N. et al. Two-stage cooperative T cell receptor-peptide major histocompatibility complex-CD8 trimolecular interactions amplify antigen discrimination. *Immunity* **34**, 13–23 (2011).

14. Casas, J. et al. Ligand-engaged TCR is triggered by Lck not associated with CD8 coreceptor. *Nat. Commun.* **5**, 5624 (2014).

15. Liu, B. et al. 2D TCR-pMHC-CD8 kinetics determines T-cell responses in a self-antigen-specific TCR system. *Eur. J. Immunol.* **44**, 239–250 (2014).

16. Hong, J. et al. A TCR mechanotransduction signaling loop induces negative selection in the thymus. *Nat. Immunol.* **19**, 1379–1390 (2018).

17. Crawford, F., Kozono, H., White, J., Marrack, P. & Kappler, J. Detection of antigen-specific T cells with multivalent soluble Class II MHC covalent peptide complexes. *Immunity* **8**, 675–682 (1998).

18. Glassman, C. R., Parrish, H. L., Lee, M. S. & Kuhns, M. S. Reciprocal TCR-CD3 and CD4 engagement of a nucleating pMHCII stabilizes a functional receptor macrocomplex. *Cell Rep.* **22**, 1263–1275 (2018).

19. Chesla, S. E., Selvaraj, P. & Zhu, C. Measuring two-dimensional receptor-ligand binding kinetics by micropipette. *Biophys. J.* **75**, 1553–1572 (1998).

20. Huang, J. et al. The kinetics of two-dimensional TCR and pMHC interactions determine T-cell responsiveness. *Nature* **464**, 932–U156 (2010).

21. Deng, L. et al. Structural basis for the recognition of mutant self by a tumor-specific, MHC class II-restricted T cell receptor. *Nat. Immunol.* **8**, 398–408 (2007).

22. Huang, J., Edwards, L. J., Evavold, B. D. & Zhu, C. Kinetics of MHC-CD8 interaction at the T cell membrane. *J. Immunol.* **179**, 7653–7662 (2007).

23. Zhu, C. & Williams, T. E. Modeling concurrent binding of multiple molecular species in cell adhesion. *Biophys. J.* **79**, 1850–1857 (2000).

24. Williams, T. E., Selvaraj, P. & Zhu, C. Concurrent binding to multiple ligands: kinetic rates of CD16b for membrane-bound IgG1 and IgG2. *Biophys. J.* **79**, 1858–1866 (2000).

25. Williams, T. E., Nagarajan, S., Selvaraj, P. & Zhu, C. Concurrent and independent binding of Fcgamma receptors IIa and IIIb to surface-bound IgG. *Biophys. J.* **79**, 1867–1875 (2000).

26. Chen, W., Evans, E. A., McEver, R. P. & Zhu, C. Monitoring receptor-ligand interactions between surfaces by thermal fluctuations. *Biophys. J.* **94**, 694–701 (2008).

27. Liu, B., Chen, W., Evavold, B. D. & Zhu, C. Accumulation of dynamic catch bonds between TCR and agonist Peptide-MHC triggers T cell signaling. *Cell* **157**, 357–368 (2014).

28. Marshall, B. T. et al. Direct observation of catch bonds involving cell-adhesion molecules. *Nature* **423**, 190–193 (2003).

29. Kao, H. & Allen, P. M. An antagonist peptide mediates positive selection and CD4 lineage commitment of MHC class II-restricted T cells in the absence of CD4. *J. Exp. Med.* **201**, 149–158 (2005).

30. Rothemund, P. W. Folding DNA to create nanoscale shapes and patterns. *Nature* **440**, 297–302 (2006).

31. Williams, T. E., Nagarajan, S., Selvaraj, P. & Zhu, C. Quantifying the impact of membrane microtopology on effective two-dimensional affinity. *J. Biol. Chem.* **276**, 13283–13288 (2001).

32. Li, Q.-J. et al. CD4 enhances T cell sensitivity to antigen by coordinating Lck accumulation at the immunological synapse. *Nat. Immunol.* **5**, 791–799 (2004).

33. Natarajan, K. et al. An allosteric site in the T-cell receptor Cbeta domain plays a critical signalling role. *Nat. Commun.* **8**, 15260 (2017).

34. He, Y. et al. Peptide-MHC binding reveals conserved allosteric sites in MHC Class I- and Class II-Restricted T Cell Receptors (TCRs). *J. Mol. Biol.* **432**, 166697 (2020).

35. Rangarajan, S. et al. Peptide-MHC (pMHC) binding to a human antiviral T cell receptor induces long-range allosteric communication between pMHC- and CD3-binding sites. *J. Biol. Chem.* **293**, 15991–16005 (2018).

36. Zhu, C., Chen, W., Lou, J., Rittase, W. & Li, K. Mechanosensing through immunoreceptors. *Nat. immuol.* **20**, 1269–1278 (2019).

37. Li, K. et al. PD-1 suppresses TCR-CD8 cooperativity during T-cell antigen recognition. *Nat. Commun.* **12**, 2746 (2021).

38. Rudd, C. E., Trevillyan, J. M., Dasgupta, J. D., Wong, L. L. & Schlossman, S. F. The CD4 receptor is complexed in detergent lysates to a protein-tyrosine kinase (pp58) from human T lymphocytes. *Proc. Natl Acad. Sci. USA* **85**, 5190–5194 (1988).

39. Burgess, K. E. et al. Biochemical identification of a direct physical interaction between the CD4:p56lck and Ti(TcR)/CD3 complexes. *Eur. J. Immunol.* **21**, 1663–1668 (1991).

40. Duplay, P., Thome, M., Herve, F. & Acuto, O. P56(Lck) interacts via its Src Homology-2 Domain with the Zap-70 Kinase. *J. Exp. Med.* **179**, 1163–1172 (1994).

41. Thome, M., Germain, V., DiSanto, J. P. & Acuto, O. The p56lck SH2 domain mediates recruitment of CD8/p56lck to the activated T cell receptor/CD3/zeta complex. *Eur. J. Immunol.* **26**, 2093–2100 (1996).

42. Chen, W., Zarnitsyna, V. I., Sarangapani, K. K., Huang, J. & Zhu, C. Measuring receptor-ligand binding kinetics on cell surfaces: from adhesion frequency to thermal fluctuation methods. *Cell Mol. Bioeng.* **1**, 276–288 (2008).

43. Evans, E., Leung, A., Heinrich, V. & Zhu, C. Mechanical switching and coupling between two dissociation pathways in a P-selectin adhesion bond. *Proc. Natl Acad. Sci. USA* **101**, 11281–11286 (2004).

44. Buckley, C. D. et al. Cell adhesion. The minimal cadherin-catenin complex binds to actin filaments under force. *Science* **346**, 1254211 (2014).
45. Bell, G. Models for the specific adhesion of cells to cells. *Science* **200**, 618–627 (1978).

Author contributions
M.N.R., V.P., C.Z., and Y.K. conceived and designed the study; C.Z. and Y.K. directed the study; M.N.R., V.P., K.L., H.-K.C., J.H., F.G., and P.A. performed experiments; C.Z. and S.T. developed mathematical models; S.T. analyzed data using mathematical model; R.A.M. provided critical reagents; M.N.R., V.P., K.L. Y.K., and C.Z. wrote the paper with contributions from other authors.

Competing interests
The authors declare no competing interests.

Additional information
Supplementary information The online version contains supplementary material available at https://doi.org/10.1038/s41467-022-34587-w.

Correspondence and requests for materials should be addressed to Yonggang Ke or Cheng Zhu.

Peer review information *Nature Communications* thanks Wolfgang Schamel and the other, anonymous, reviewer(s) for their contribution to the peer review of this work.

Reprints and permissions information is available at http://www.nature.com/reprints

Publisher's note Springer Nature remains neutral with regard to jurisdictional claims in published maps and institutional affiliations.